The Astrophysical Journal, 760:131 (25pp), 2012 December 1 doi:10.1088/0004-637X/760/2/131

THE DEPENDENCE OF QUENCHING UPON THE INNER STRUCTURE OF GALAXIES AT $0.5 \leqslant z < 0.8$ IN THE DEEP2/AEGIS SURVEY

Edmond Cheung[1], S. M. Faber[1,2], David C. Koo[1,2], Aaron A. Dutton[3], Luc Simard[4], Elizabeth J. McGrath[1], J.-S. Huang[5], Eric F. Bell[6], Avishai Dekel[7], Jerome J. Fang[1], Samir Salim[8], G. Barro[1], K. Bundy[9], A. L. Coil[10], Michael C. Cooper[11,21], C. J. Conselice[12], M. Davis[13], A. Domínguez[14], Susan A. Kassin[15,22], Dale D. Kocevski[1], Anton M. Koekemoer[16], Lihwai Lin[17], Jennifer M. Lotz[8], J. A. Newman[18], Andrew C. Phillips[1], D. J. Rosario[19], Benjamin J. Weiner[20], and C. N. A. Willmer[20]

[1] Department of Astronomy and Astrophysics, 1156 High Street, University of California, Santa Cruz, CA 95064, USA; ec2250@gmail.com
[2] UCO/Lick Observatory, University of California, 1156 High Street, Santa Cruz, CA 95064, USA
[3] Department of Physics and Astronomy, Elliot Building, 3800 Finnerty Road, University of Victoria, Victoria, BC V8P 5C2, Canada
[4] Herzberg Institute of Astrophysics, National Research Council of Canada, 5071 West Saanich Road, Victoria, BC V9E 2E7, Canada
[5] Harvard-Smithsonian Center for Astrophysics, 60 Garden State, Cambridge, MA 02138, USA
[6] Department of Astronomy, University of Michigan, 500 Church St., Ann Arbor, MI 48109, USA
[7] Racah Institute of Physics, The Hebrew University, Jerusalem 91904, Israel
[8] National Optical Astronomical Observatories, 950 N. Cherry Avenue, Tucson, AZ 85719, USA
[9] Kavli Institute for the Physics and Mathematics of the Universe, University of Tokyo, Kashiwa 277-8582, Japan
[10] Department of Physics, Center for Astrophysics and Space Sciences, University of California at San Diego, 9500 Gilman Dr., La Jolla, San Diego, CA 92093, USA
[11] Center for Galaxy Evolution, Department of Physics and Astronomy, University of California, Irvine, 4129 Frederick Reines Hall, Irvine, CA 92697, USA
[12] School of Physics and Astronomy, University of Nottingham, Nottingham NG7 2RD, UK
[13] Department of Astronomy, University of California, Berkeley, CA 94720, USA
[14] Department of Physics and Astronomy, University of California, Riverside, CA 92521, USA
[15] Astrophysics Science Division, Goddard Space Flight Center, Code 665, Greenbelt, MD 20771, USA
[16] Space Telescope Science Institute, 3700 San Martin Drive, Baltimore, MD 21218, USA
[17] Institute of Astronomy and Astrophysics, Academia Sinica, Taipei 106, Taiwan
[18] Department of Physics and Astronomy, University of Pittsburgh, 3941 O'Hara Street, Pittsburgh, PA 15260, USA
[19] Max Planck Institute for Extraterrestrial Physics, P.O. Box 1312, Giessenbachstrasse, D-85741 Garching, Germany
[20] Steward Observatory, 933 N. Cherry Street, University of Arizona, Tucson, AZ 85721, USA
Received 2012 April 5; accepted 2012 October 11; published 2012 November 16

ABSTRACT

The shutdown of star formation in galaxies is generally termed "quenching." Quenching may occur through a variety of processes, e.g., active galactic nucleus (AGN) feedback, stellar feedback, or the shock heating of gas in the dark matter halo. However, which mechanism(s) is, in fact, responsible for quenching is still in question. This paper addresses quenching by searching for traces of possible quenching processes through their effects on galaxy structural parameters such as stellar mass (M_*), M_*/r_e, surface stellar mass density ($\sim M_*/r_e^2$), and Sérsic index (n). We analyze the rest-frame $U-B$ color correlations versus these structural parameters using a sample of galaxies in the redshift range $0.5 \leqslant z < 0.8$ from the DEEP2/AEGIS survey. In addition to global radii, stellar masses, and Sérsic parameters, we also use "bulge" and "disk" photometric measurements from GIM2D fits to *HST*/ACS V and I images. We assess the tightness of the color relationships by measuring their "overlap regions," defined as the area in color-parameter space in which red and blue galaxies overlap; the parameter that minimizes these overlap regions is considered to be the most effective color discriminator. We find that Sérsic index (n) has the smallest overlap region among all tested parameters and resembles a step function with a threshold value of $n = 2.3$. There exists, however, a significant population of outliers with blue colors yet high n values that seem to contradict this behavior; they make up ≈40% of $n > 2.3$ galaxies. We hypothesize that their Sérsic values may be distorted by bursts of star formation, AGNs, and/or poor fits, leading us to consider central surface *stellar mass density*, $\Sigma^*_{1\,\mathrm{kpc}}$, as an alternative to Sérsic index. Not only does $\Sigma^*_{1\,\mathrm{kpc}}$ correct the outliers, but it also forms a tight relationship with color, suggesting that the *innermost structure of galaxies is most physically linked with quenching*. Furthermore, at $z \sim 0.65$, the majority of the blue cloud galaxies cannot simply fade onto the red sequence since their GIM2D bulge masses are only half as large on average as the bulge masses of similar red sequence galaxies, thus demonstrating that stellar mass must absolutely increase at the centers of galaxies as they quench. We discuss a two-stage model for quenching in which galaxy star formation rates are controlled by their dark halos while they are still in the blue cloud and a second quenching process sets in later, associated with the central stellar mass buildup. The mass buildup is naturally explained by any non-axisymmetric features in the potential, such as those induced by mergers and/or disk instabilities. However, the identity of the second quenching agent is still unknown. We have placed our data catalog online.

Key words: galaxies: bulges – galaxies: evolution – galaxies: formation – galaxies: fundamental parameters – galaxies: structure

Online-only material: color figures

1. INTRODUCTION

With the advent of large galaxy surveys, the color bimodality of the galaxy population has become well characterized (Lin et al. 1999; Strateva et al. 2001; Im et al. 2002; Blanton et al. 2003; Kauffmann et al. 2003; Bell et al. 2004b). Galaxy counts back in time revealed that the number of red galaxies has at least doubled since $z \sim 1$ while the number of blue galaxies has remained relatively constant (Bell et al. 2004b; Bundy et al. 2006; Faber et al. 2007; Arnouts et al. 2007; Brown et al. 2007; Ilbert et al. 2010; Domínguez et al. 2011; Gonçalves et al. 2012). A natural interpretation is that galaxies evolve from blue to red with time, i.e., from star forming to "quenched." Later measurements of star formation rates confirmed that blue galaxies create stars at a high rate while red galaxies show little to no star formation (Salim et al. 2005, 2007; Noeske et al. 2007; Zheng et al. 2007). Moreover, star formation rates in blue galaxies correlate well with stellar mass, forming the "Main Sequence" of star formation. In non-dusty red galaxies, however, star formation is generally much lower than that of blue ones (Salim et al. 2005). This abrupt jump in star formation rate across colors motivates the search for a quenching process. For simplicity, we define quenching to be a process that permanently turns a blue star-forming galaxy into a red non-star-forming one.[23]

Many quenching mechanisms have been proposed, but they can generally be categorized into two classes. The first class is internal processes; these act to either expel the gas already in a galaxy or render it inert to star formation. Examples of internal processes include feedback from starbursts and active galactic nuclei (AGNs), both of which may be triggered by mergers. They act to heat the surrounding gas and/or drive winds out of the galaxy (e.g., Sanders et al. 1988; Springel et al. 2005; Murray et al. 2005; Cox et al. 2008; Ciotti et al. 2009; Alexander et al. 2010). Another example of an internal process is morphological quenching (Martig et al. 2009). In this model, the presence of a dominant bulge stabilizes the gaseous disk against gravitational instabilities needed for star formation.

The second class contains external processes, which we define as acting to prevent gas from accreting onto a galaxy in the first place. The main external process is halo mass quenching (Silk 1977; Rees & Ostriker 1977; Blumenthal et al. 1984; Birnboim & Dekel 2003; Kereš et al. 2005; Dekel & Birnboim 2006; Cattaneo et al. 2006); this posits that dark matter halos above a critical halo mass establish virial shocks that stop the flow of cold gas onto their central galaxies. Additional examples are AGN "radio mode" feedback (Croton et al. 2006) and gravitational heating (Khochfar & Ostriker 2008; Birnboim & Dekel 2011), both of which can be considered as variants of halo mass quenching since both mechanisms require massive halos.

According to our definition, mergers do not qualify as an external process since they act to exhaust and/or remove existing gas already within a galaxy. By the same token, ram pressure stripping (Gunn & Gott 1972) is also not considered an external process since it strips gas from a galaxy. Furthermore, this paper only concentrates on quenching processes that affect the central galaxy of a halo. According to Gerke et al. (2005), who used a sample of DEEP2 galaxies (∼25% of the total DEEP2 sample), only ∼32% of DEEP2 galaxies are in groups, meaning that ∼68% of these galaxies are in the field. These field galaxies would be centrals, and additionally, since each group contains one central, the percentage of centrals in this DEEP2 sample is at least ∼68%. Assuming that this sample is representative of the entire DEEP2 data set, we can conclude that most of our galaxies are centrals. Thus, we will not consider mechanisms that affect satellites, i.e., strangulation and harassment (Larson et al. 1980; Moore et al. 1996).

These quenching processes may imprint themselves on the structure of a galaxy, e.g., major mergers can create highly concentrated galaxies. The prospect of detecting quenching mechanisms at work via observable changes in structural parameters has motivated many previous works. One of the first parameters explored was luminosity. Using an early Sloan Digital Sky Survey (SDSS) sample, Strateva et al. (2001) found that galaxies are bimodal in color, i.e., galaxies generally lie within the red sequence or the blue cloud. However, while galaxies are well separated in color, they overlap over almost the entire range of luminosity, indicating that luminosity is not the main driver of galaxy color.

Later, stellar mass was explored; hereafter, mass refers to stellar mass unless otherwise stated. For a sample of local SDSS galaxies, Kauffmann et al. (2003) found that the correlations between the star formation history indicators $D_n(4000)$ and $H\delta_A$ (which can also be thought of as a proxy for galaxy color) and mass are significantly better than that of the g-band luminosity. They further found that galaxies divide into two distinct families at a stellar mass of $3 \times 10^{10}\ M_\odot$.

Recently, additional structural parameters have been introduced. Using an SDSS sample, Kauffmann et al. (2006) found that the galaxy surface mass density ($\sim M_*/r_e^2$) produced an even sharper division in specific star formation rate (SSFR) than stellar mass (see also Brinchmann et al. 2004; Maier et al. 2009). They suggested that high surface stellar mass density is connected to the creation of a bulge and the quenching of a galaxy.

Franx et al. (2008) intercompared several of the aforementioned color-parameter correlations in the redshift range $0 < z < 3$ using data from the FIREWORKS catalog (Wuyts et al. 2008). Confirming the Kauffmann et al. (2006) result, they showed that surface mass density better separates red and blue galaxies than stellar mass alone. Franx et al. (2008) also examined a second structural parameter, the "inferred velocity dispersion" ($\sim M_*/r_e$), and found that the inferred velocity dispersion also better distinguishes red and blue galaxies than mass.

Besides these structural parameters, Sérsic index (n) has also been explored. Driver et al. (2006) and Allen et al. (2006) observed a clear bimodal distribution in both the rest-frame $u-r$ color and n in the Millennium Galaxy Catalog. A similar trend with SDSS galaxies was seen by Blanton et al. (2003) and Schiminovich et al. (2007). Bell (2008) showed that n is an even better color discriminator than surface mass density. However, several outliers were noted, and he concluded that high n is a necessary (but not sufficient) condition for quiescence. Recently, Wuyts et al. (2011) and Bell et al. (2012) found that the correlation between quenching and n was in place since at least $z \sim 2.5$.

A study by Mendez et al. (2011) supports the implications of the relationship between Sérsic index and quiescence. Using a sample of DEEP2/AEGIS galaxies at $0.4 < z < 1.2$, they compared the morphological parameters (CAS, G/M_{20}, and

[21] Hubble Fellow.
[22] NASA Postdoctoral Program Fellow.
[23] Rejuvenation of star formation in quiescent spheroids through gas and/or satellite infall has been proposed to explain the observed blue spheroids seen in various works (e.g., Kannappan et al. 2009; Schawinski et al. 2009). In this paper, we do not consider this process.

B/T) of galaxies in the green valley—galaxies with colors that lie between the blue and the red peak in the color bimodality—to those in the blue cloud and the red sequence. They found that most green valley galaxies are still disks but are building up their central bulge, in that they have higher concentrations and higher B/T ratios than blue galaxies and less than red galaxies. In other words, they found that the bulges of galaxies are being created or augmented in the evolution of a galaxy from the blue cloud, through the green valley, and finally onto the red sequence.

A recent study by Wake et al. (2012b) adds SDSS central velocity dispersion to the list of previously considered structural parameters. It is also the first study to compare the efficacy of Sérsic indices head to head versus other variables. They find that central velocity dispersion leaves the weakest residual color trends with other parameters and conclude that quenching correlates most strongly with central velocity dispersion.

The dependence of quiescence on halo properties has thus far been measured only *statistically*, by looking at the probability that a galaxy is quenched as a function of some mass and/or surrounding density. Peng et al. (2010) found that just two processes—"stellar mass quenching," which correlates directly with galaxy stellar mass, and "environmental quenching," which correlates directly with local environmental density—can accurately describe the quenching probabilities of SDSS galaxies. A later paper (Peng et al. 2012) divided centrals from satellites and found that central quenching—of relevance here—had no environment dependence but related only to stellar mass. A similar study by Woo et al. (2012) introduced halo mass, which Peng et al. (2010) had not considered, and found that central quenching correlated better with halo mass than with stellar mass. However, it is important to note that, regardless of whether halo mass is better than stellar mass, it is clearly *not* as predictive as structural variables such as Sérsic index or central velocity dispersion. We expound on this statement in the discussion of this paper, but a cursory examination of the SSFR as a function of halo mass from Conroy & Wechsler (2009) (Figure 8) shows that star formation only gradually changes as a function of halo mass, whereas the plots of color as a function of Sérsic index and central velocity dispersion from Wake et al. (2012b) (Figure 1) show that color changes quite sharply as a function of both these parameters. Thus, a central challenge has emerged for the halo mass quenching picture, namely, why do galaxy structural parameters predict the outcome of halo mass quenching better than halo mass itself does? We return to this question below.

While correlations do not necessarily imply causality, they are strong hints, all of which has led to a rather complicated picture of galaxy evolution. Quenching may well involve a mix of complex processes that are likely to be dependent on several parameters that are themselves correlated. However, several themes emerge from the results discussed. The conditions of the bulge and perhaps the very center of the galaxy appear to be important. Indeed, Kauffmann et al. (2006) suggested that bulge building is the underlying cause of their correlation between color and surface mass density. And several authors, cited above, concluded that high n is necessary to quench a galaxy, providing further evidence for bulges. Moreover, since a hallmark of bulges is high central density, it is notable that Wake et al. (2012b) find that central velocity dispersion is the single most correlated parameter of all with galaxy color. And finally, since bulges and high central densities are closely associated with black holes (Magorrian et al. 1998; Gebhardt et al. 2000), it is tempting to conclude that this mounting chain of evidence is simply a "smoking gun" pointing to AGN feedback.

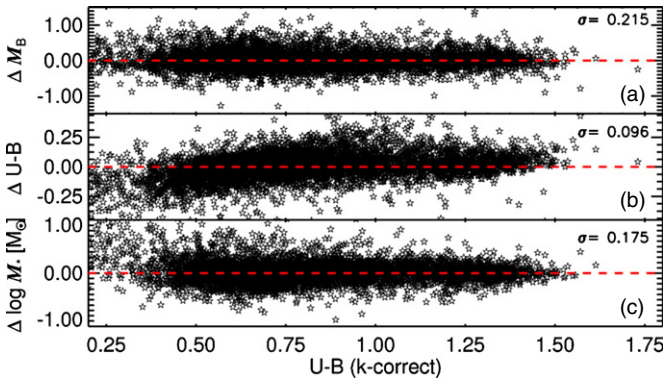

Figure 1. We plot the residuals of rest-frame absolute B-band magnitude M_B, rest-frame $U-B$, and stellar mass M_* against rest-frame $U-B$ from k-correct. Panel (a) shows the difference between M_B computed from k-correct v4.2 (Blanton & Roweis 2007) using CFHT BRI and redshift and M_B computed from Equations (3) and (4). Panel (b) plots the residuals of $U-B$ from k-correct to $U-B$ from Equation (5). Panel (c) shows the residuals of M_* from J. Huang et al. (2012, in preparation) and M_* obtained using Equations (3) and (6). From the one-to-one red dashed line in each panel, it is clear that values derived from our fits are consistent with the fiducial values. The dispersion σ is displayed on the top of each panel.

(A color version of this figure is available in the online journal.)

In total, these works suggest that internal processes, and specifically *central* processes, are responsible for shutting down star formation. As noted, this poses a problem at first sight for halo mass quenching, since halo properties are seen to correlate more weakly with quenching than do variables such as Sérsic index and central velocity dispersion. However, a key element in the halo picture is radio mode, which depends on AGN feedback (Dekel & Birnboim 2006; Croton et al. 2006) and thus possibly on internal/central conditions. Perhaps it will be possible to link these various processes in a plausible causative chain that explains all of the data. We return to this possibility in the discussion section.

In this paper, we build on previous works and consider the possibility of multiple physical processes acting together in concert to quench star formation in galaxies. Whereas most works have only explored global structural parameters, we explore both global and *central* structural parameters. Our data set is AEGIS galaxies possessing *HST*/ACS imaging, similar to Mendez et al. (2011) but over a narrower redshift range, $0.5 \leqslant z < 0.8$. Like them, we use color as a proxy for quenching and structural parameters derived from the same GIM2D fits. However, we focus on different structural parameters and, importantly, convert luminous quantities of subcomponents to stellar mass using color-derived M/L ratios.

Our ultimate goal is to identify that parameter, or combination of parameters, that seems to be the best discriminant between star-forming and quenched galaxies. Having found that combination, we compare its efficacy (or sharpness) to studies focusing on halo parameters (e.g., Woo et al. 2012) in order to assess whether the primary driver of quenching is conditions that exist inside a galaxy or outside it.

A major result of this paper is that the Sérsic index, n, displays the sharpest break between star-forming and quenched galaxies, i.e., it looks most like a quenching threshold. However, n does not really distinguish red and blue galaxies all that well—≈40% of AEGIS galaxies with high n have blue colors. Suspecting contamination from starbursts, AGNs, or errors of measurement,

we introduce a novel parameter that is closely related to n but is more robustly measured, namely, central surface mass density, $\Sigma^*_{1\,\mathrm{kpc}}$. Under this parameter, we find that the number of outliers is dramatically reduced, implying that the innermost structure of galaxies may be most fundamentally related to quenching. Moreover, using stellar mass measurements of the bulge and inner 1 kpc region of galaxies, we show that at $z \sim 0.65$, most blue galaxies cannot simply fade onto the red sequence; they must instead undergo a *significant restructuring* of their innermost stellar density profiles en route to quenching.

These results are compared to various theoretical models. The first major conclusion is that the quenching sharpness found with our new parameter, central surface mass density, far exceeds that found with halo mass, highlighting a major tension with the halo quenching picture. Looking at alternative theories, we find several striking points of agreement with the major-merger picture, but also some important caveats. These concerns suggest that bulge building may just proceed quite naturally because galaxies at these redshifts are not yet very axisymmetric and non-central torques are constantly being generated. Finally, the very close connection between quenching state and central conditions that we find in this paper looks like a "smoking gun" for AGN feedback, yet not all aspects of the data are fully explained by that model either.

Finally, we place online[24] one of the most comprehensive data sets available, composed of 11,223 galaxies at $0.2 < z < 1.2$, with a mean redshift of $z \sim 0.75$. One powerful aspect of this data set is the use of multi-color *HST*/ACS *V*- and *I*-band imaging, which allows the accurate conversion of light to stellar mass. It also includes GIM2D bulge-disk decompositions (Simard et al. 2002), which provide photometric and structural measurements of the bulges and disks separately; these intermediate-redshift galaxy decompositions are only possible thanks to the high-resolution *Hubble Space Telescope* (*HST*) imaging. Additionally, stellar masses are derived for the subcomponents using their V, I colors.

This paper is organized as follows: Section 2 describes our data and derivation of the analyzed quantities. In Section 3, we explain our sample selection criteria and discuss sample completeness. Section 4 presents our main results—the correlations between structural parameters and color. In Section 5, we compare our results with several theoretical models and present our two-stage scenario of galaxy evolution. Finally, we list our conclusions in Section 6. A cosmology with $H_0 = 70\ \mathrm{km\ s^{-1}\ Mpc^{-1}}$, $\Omega_m = 0.30$, and $\Omega_\Lambda = 0.70$ is used throughout this paper. All magnitudes are on the AB system.

2. DATA

We start with a description of all the main sources of data used in this paper, which come from AEGIS, and then discuss the sample selection in Section 3. For an overview of the AEGIS data, please see Davis et al. (2007).

2.1. CFHT BRI Photometric Catalog

The first photometric data are those we use from the Canada–France–Hawaii Telescope (CFHT) *BRI* imaging catalog. The CFHT 12k camera has a 12,288 × 8192 pixel CCD mosaic array and a plate scale of $0\farcs207\ \mathrm{pixel^{-1}}$, providing a field of view of $0\fdg70 \times 0\fdg47$. Five separate fields, with one to five distinct CFHT 12k pointings per field, were observed from 1999 September to 2000 October. The integration time for each point was ∼1 hr in *B* and *R* and ∼2 hr in *I*, broken down to individual exposures of 600 s. The data are complete to ∼25.25 in *B*, 24.75 in *R*, and ∼24.25 in *I* (see Coil et al. 2004 for more details).

These *BRI* magnitudes were used with *k*-correct v4.2 (Blanton & Roweis 2007) to obtain the rest-frame color $(U-B)$ and absolute magnitudes (M_B) used throughout this paper.

2.2. HST ACS V+I Imaging and SExtractor Photometry

The main photometric catalog from which the sample was selected is based on *HST*/ACS images taken as part of the AEGIS survey (Davis et al. 2007) under program GO-10134 (PI: M. Davis). The exposures were taken between 2004 June and 2005 March over 63 tiles covering an area approximately $10\farcm1 \times 70\farcm5$ in size. Each tile was observed for a single orbit in F606W (*V*) and F814W (*I*) using a four-point dither pattern. These pointings were combined with the STSDAS Multidrizzle package using a square kernel. The final images have a pixel scale of $0\farcs03\ \mathrm{pixel^{-1}}$ and a point-spread function (PSF) of $0\farcs12$ FWHM. The 5σ limiting magnitudes for a point source are $V = 28.14$ and $I = 27.52$ within a circular aperture of radius $0\farcs12$ (∼50 pixel area). For an extended object, the 5σ limiting magnitudes are $V = 26.23$ and $I = 25.61$ for a circular aperture of radius $0\farcs3$ (∼314 pixel area).

SExtractor (Bertin & Arnouts 1996) is used to detect objects in summed Advanced Camera for Surveys (ACS) *V*+*I* images and to construct initial galaxy segmentation maps. A detection threshold of 1.5σ and 50 pixels is chosen. These detection maps and the ACS zero points (Sirianni et al. 2005) were applied to each band separately to create the ACS photometric catalogs. We selected all nonstellar objects with SExtractor CLASS_STAR < 0.9 and $I < 25.0$ that did not lie within 50 pixels of a tile edge for our automated morphology analysis, covering an effective area of 710.9 $\mathrm{arcmin^2}$ in the ACS images (see Lotz et al. 2008a, for more details).

This high-resolution catalog was used to generate the galaxy sample composing the GIM2D bulge+disk catalogs.

2.3. GIM2D

Structural parameters of the *HST*/ACS imaged galaxies were measured using GIM2D, a 2D bulge+disk decomposition program (Simard et al. 2002). Three separate fits were made: a single Sérsic fit with floating n, a bulge + disk fit with $n_{\mathrm{bulge}} = 2$ and $n_{\mathrm{disk}} = 1$, and a bulge + disk fit with $n_{\mathrm{bulge}} = 4$ and $n_{\mathrm{disk}} = 1$ The three fits were done simultaneously using both the *V* and *I* *HST*/ACS images according to the procedure in Simard et al. (2002). The bulge surface brightness profile is parameterized by

$$\Sigma(r) = \Sigma_{\mathrm{e}} \exp\{k[(r/r_{\mathrm{e}})^{1/n} - 1]\} \quad (1)$$

as given by Sersic (1968). Here, the parameter k is set equal to $1.9992n - 0.3271$, so r_{e} remains the projected radius enclosing half the light (Capaccioli 1989). The disk profile is a simple exponential:

$$\Sigma(r) = \Sigma_0 \exp(-r/r_{\mathrm{d}}), \quad (2)$$

where Σ_0 is the face-on central surface brightness and r_{d} is the semimajor axis scale length. For the single Sérsic fit, Equation (1) is used to fit the whole galaxy.

GIM2D also measures concentration, which, unlike the SDSS definition, is defined as the ratio of the inner and outer isophote fluxes of normalized radii α and 1; we follow Abraham et al.

[24] http://people.ucsc.edu/∼echeung1/data.html

(1994) and use $\alpha = 0.3$. Additionally, the GIM2D models produce galaxy, bulge, and disk V, I magnitudes—these are the primary magnitudes used throughout this paper.

Throughout this paper, most of our results utilize the single Sérsic fits (Table 3). When examining the bulge and disk properties, we use the best-fitting, two-component decomposition, i.e., either $n_{\rm bulge} = 4$ or $n_{\rm bulge} = 2$ (Tables 4 and 5), for each galaxy as indicated by χ^2. We only use bulge measurements of $B/T > 0.1$ galaxies, as the low signal-to-noise ratio (S/N) makes measurements of systems with $B/T < 0.1$ uncertain. Our subcomponent sample with GIM2D measurements of the bulge and disk separately is composed of ≈60% from the $n_{\rm bulge} = 2$ and ≈40% from the $n_{\rm bulge} = 4$ fits. Comparing the $n_{\rm bulge} = 4$ fit to the $n_{\rm bulge} = 2$ fit shows a median offset of $\log M_{*,\rm bulge}$ to be ≈0.10 dex with a dispersion of ≈0.23 dex while $\log r_{\rm e,bulge}$ has a median offset of ≈0.15 dex with a dispersion of ≈0.28 dex; both parameters are offset toward higher values in the $n_{\rm bulge} = 4$ fit.

2.4. DEEP2 + DEEP3 Redshift Survey

Spectroscopic redshifts were measured in the DEEP2 redshift survey using the DEIMOS spectrograph (Faber et al. 2003) on the Keck II telescope (Davis et al. 2003; Newman et al. 2012). Targets were selected for DEEP2 spectroscopy from the CFHT *BRI* imaging described in Section 2.1. Most of DEEP2 used the *BRI* photometry to screen out low-redshift galaxies, but this screening was not applied in the AEGIS region, and so the resulting sample is representative from $z = 0$ to $z \sim 1.4$. Eligible targets must have $18.5 \leqslant R \leqslant 24.1$ and surface brightness brighter than $\mu_R \leqslant 26.5$ (Davis et al. 2003; Newman et al. 2012).

Additional spectroscopic redshifts are available in the recently completed DEEP3 redshift survey (Cooper et al. 2011, 2012). This survey shares many of the same characteristics of DEEP2, i.e., they both use the DEIMOS spectrograph and were both preselected using CFHT *BRI* photometry. However, while DEEP2 used a 1200 line mm^{-1} grating in DEIMOS, DEEP3 employed a 600 line mm^{-1} grating, resulting in spectra of lower resolution. The quality of the redshifts, however, is unaffected.

Taking only spectroscopic redshifts with quality code of $Q = 3$ or $Q = 4$ and cross-matching it to the *HST*/ACS catalog yields a sample of 6310 galaxies; these galaxies make up the spectroscopic sample.

2.5. Photometric Redshifts

The DEEP2+DEEP3 survey is approximately 65% complete to $R = 24.1$ in AEGIS (Newman et al. 2012). For those galaxies without spectroscopic z and to extend the sample to fainter limits, we utilized photometric redshifts (J. Huang et al. 2012, in preparation) derived from the Artificial Neural Networks method (Collister & Lahav 2004) using the multi-wavelength AEGIS photometry that includes 12 unique bands in the wavelength range from u to 8 μm, with deep *Spitzer*/IRAC photometry (Davis et al. 2007; Barmby et al. 2008; X. Z. Zheng et al. 2012, in preparation) as the base. This sample was 3.6 μm selected ($f_{3.6} > 2$ μJy) with a color cut to isolate $z < 1.5$ galaxies. The redshift catalog is complete down to $\log M_*/M_\odot = 9.5$ for $0.4 < z < 1.2$, and the rms accuracy is $\Delta z/(1+z) = 0.025$. Cross-matching this sample to the *HST*/ACS catalog that does not have a quality spectroscopic redshift yields 4913 galaxies; these galaxies make up the photometric sample. The total number of galaxies in our initial sample, consisting of the spectroscopic and photometric sample, is 11,223.

2.6. Rest-frame Absolute B Magnitudes and $U-B$ Colors

Rest-frame absolute M_B magnitudes and $U-B$ colors are needed for both integrated galaxies and bulge and disk subcomponents separately. For galaxies, these quantities are obtained through k-correct v4.2 (k-corrected down to $z = 0$; Blanton & Roweis 2007) with CFHT *BRI* photometry and redshift as inputs.

For bulges and disks, however, CFHT *BRI* photometry is not available, but there is *HST*/ACS V and I photometry modeled by GIM2D. In order to be consistent with the galaxy values, we derive a calibration for M_B and $U-B$ from V, I, and redshift. We use the galaxy rest-frame magnitudes from k-correct as fiducial values to derive this calibration, which was then used to calculate M_B and $U-B$ for the subcomponent sample.

The functional form we use for M_B is (Gebhardt et al. 2003)[25]

$$M_B = I_{814} - DM(\Omega_m, \Omega_\Lambda, \Omega_K) + K_{\rm IB}, \quad (3)$$

where DM is the distance modulus for the adopted cosmology and

$$\begin{aligned} K_{\rm IB} = {} & 1.490 - 18.266z + 94.056z^2 \\ & - 229.782z^3 + 294.741z^4 - 189.892z^5 + 48.034z^6 \\ & + (2.233 - 5.448z + 3.187z^2 - 0.082z^3)(V-I) \\ & + (0.592 - 0.540z - 0.036z^2)(V-I)^2. \end{aligned} \quad (4)$$

The functional form for $U-B$ is (Gebhardt et al. 2003)

$$\begin{aligned} U-B = {} & -0.882 + 16.627z - 84.798z^2 \\ & + 212.831z^3 - 286.211z^4 + 195.256z^5 - 52.584z^6 \\ & + (0.492 + 0.380z + 0.415z^2 - 0.493z^3)(V-I) \\ & + (0.751 - 1.609z + 0.739z^2)(V-I)^2. \end{aligned} \quad (5)$$

Figures 1(a) and (b) compare the values of M_B and $U-B$ from Equations (3)–(5) to those derived from k-correct. The relations are nicely linear with $\sigma(M_B) = 0.215$ mag and $\sigma(U-B) = 0.096$ mag. We use these relations to compute M_B and $U-B$ for the subcomponent sample. We also use these equations for the galaxies in our sample that have ill-measured CFHT *BRI* measurements, characterized by large errors (≈7%).

2.7. Stellar Masses

Stellar masses for most of our sample are available from J. Huang et al. (2012, in preparation). Using a Salpeter initial mass function, the multi-wavelength AEGIS photometry (with deep *Spitzer*/IRAC photometry as the base; Davis et al. 2007; Barmby et al. 2008; X. Z. Zheng et al. 2012, in preparation; J. Huang et al. 2012, in preparation) was fit to a grid of synthetic SEDs from Bruzual & Charlot (2003), assuming solar metallicity. These synthetic SEDs span a range of ages, dust content, and exponentially declining star formation histories. The typical widths of the stellar mass probability distributions are 0.1–0.2 dex.

To obtain stellar masses for the subcomponent samples, we utilize the well-known correlation between mass-to-light ratio (M_*/L) and optical colors (e.g., Bell & de Jong 2001). To account for our large redshift range, we add a redshift-dependent term to the relationship, similar to the approach in Lin et al. (2007) and Weiner et al. (2009). Options are to use either rest-frame $U-B$ (from k-correct) or observed $V-I$. To aid our choice, we make fits using both colors and compare them to the M_*/L_B values in Figure 2. The left panels display M_*/L_B

[25] We use the Gebhardt et al. (2003) form but fit for our own coefficients.

Table 1
Galaxy Properties

DEEPID	Q	z	M_B k-correct	M_B Equations (3) and (4)	$U-B$ k-correct	$U-B$ Equation (5)	M_* J. Huang et al. (2012, in preparation)	M_* Equations (6), (3), (4)
(1)	(2)	(3)	(4)	(5)	(6)	(7)	(8)	(9)
13049654	4	0.20	−17.52	−17.49	0.77	0.77	9.14	9.19
13018599	4	0.79	−20.14	−20.13	1.14	1.14	10.56	10.42
12020067	4	0.45	−19.52	−19.38	0.62	0.65	9.38	9.49
12007757	4	0.99	−20.80	−20.91	0.89	0.83	10.09	10.12
13040619	4	0.71	−20.78	−20.96	1.34	1.24	10.81	10.82
13048556	4	0.61	−20.03	−20.48	0.64	0.59	9.53	9.75
13049852	4	0.57	−20.93	−21.01	1.44	1.39	10.93	10.94
13026131	−1	0.54	−18.73	−18.55	0.79	0.89	9.51	9.46
12020067	4	0.45	−19.52	−19.38	0.62	0.65	9.38	9.49
12015606	4	0.67	−20.77	−20.85	0.78	0.88	10.27	10.36
13058131	4	0.71	−20.84	−20.98	1.34	1.32	10.74	10.90
12016156	4	0.74	−19.47	−19.57	0.48	0.57	−1.00	9.37
13012297	4	0.81	−21.26	−21.19	1.23	1.24	10.92	10.94
12007918	4	0.66	−20.47	−20.45	0.63	0.68	9.79	9.90
13011795	−1	0.71	−19.81	−19.82	1.33	1.32	10.37	10.43
13064645	4	1.21	−22.56	−22.10	1.45	0.79	11.09	11.14
12016799	3	0.68	−20.54	−20.54	1.16	1.12	10.67	10.53
12023870	−1	0.48	−18.78	−18.88	0.56	0.57	9.18	9.12
12004470	−1	0.46	−19.31	−19.15	0.29	0.53	9.13	9.17
12020439	4	0.58	−19.17	−18.97	0.74	0.66	10.03	9.27

Notes. Twenty randomly selected galaxies from the catalog are shown. The entire catalog is available at http://people.ucsc.edu/~echeung1/data.html. Column 1: unique DEEPID. Column 2: spectroscopic redshift quality code. Values of 3 and above are secure spectroscopic redshifts (see Newman et al. 2012 for more details), and they compose the spectroscopic sample. For values below 3, we use the photometric sample and their corresponding photometric redshifts. Column 3: best available redshift. Those with $Q \geqslant 3$ are spectroscopic z; those with $Q \leqslant 2$ are photometric z. Column 4: absolute B-band magnitude derived from k-correct. About 7% have large error measurements; we use vales from Column (5) for these objects. Column 5: absolute B-band magnitude derived from Equations (3) and (4). Column 6: $U-B$ rest-frame color derived from k-correct. About 7% have large error measurements; we use vales from Column (7) for these objects. Column 7: $U-B$ rest-frame color derived from Equation (5). Column 8: stellar mass from J. Huang et al. (2012, in preparation); ≈10% of our sample have no corresponding M_*; they are marked by −1.00. We use Column (9) for these objects. Column 9: stellar mass derived from Equations (6), (3), and (4).

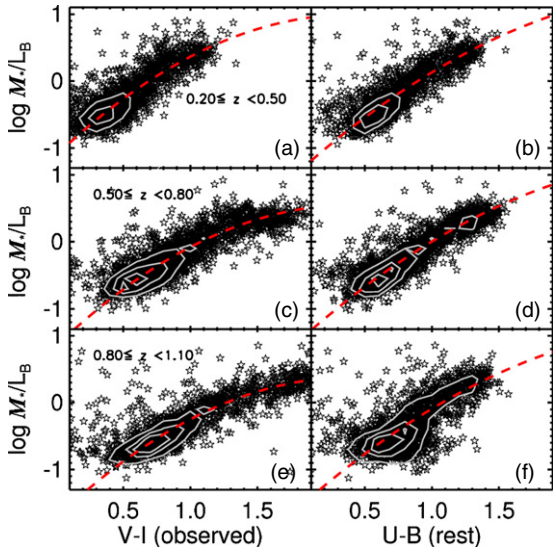

Figure 2. M_*/L_B ratio (mass from J. Huang et al. 2012, in preparation, and B-band luminosity from k-correct) vs. observed $V-I$ (left column) and rest frame $U-B$ (right column) in three redshift bins: (a) and (b) $0.20 \leqslant z < 0.50$, (c) and (d) $0.50 \leqslant z < 0.80$, and (e) and (f) $0.80 \leqslant z < 1.10$. Contours are shown to give a sense of the relative number densities. The red dashed curve in each panel represents our fit; the fit for M_*/L_B as a function of observed $V-I$ is better than the fit to rest-frame $U-B$; hence, we adopt it.

(A color version of this figure is available in the online journal.)

versus observed $V-I$, while the right panels plot M_*/L_B versus rest-frame $U-B$. Each row represents a different redshift range. Overplotted in each panel is a red dashed curve that represents our fit. The fit for M_*/L_B as a function of $V-I$ is a better match than the fit to $U-B$, especially at high redshifts. The final adopted expression for M_*/L_B is

$$\log M_*/L_B = -0.340 - 2.593z + 1.195z^2 \times 1.908(V-I) - 0.432(V-I)^2. \quad (6)$$

Together with the absolute B magnitudes measured from Equations (3) and (4), we are now in a position to calculate stellar masses for any object with a measured V, I, and redshift. These calibrated fits are used to obtain M_* values for the subcomponent samples. For the galaxies in our sample that do not have stellar masses from J. Huang et al. (2012, in preparation) (≈10%), their M_* are also obtained this way; these stellar masses are shown in Table 1. We make a final check of our method by comparing these derived stellar masses to those calculated by J. Huang et al. (2012, in preparation); this is shown in Figure 1(c), where the relationship is well behaved with an rms scatter of 0.175 dex.

2.8. Error Estimates

All error estimates measured by GIM2D, i.e., the structural parameters such as r_e and n, are 99% confidence limits (Simard et al. 2002); we convert these into 1σ limits assuming a Gaussian distribution. There are two sources of stellar mass: those from the SED fitting and those from our mass fits. The errors for the former are the typical widths of the stellar mass probability distribution (0.1–0.2 dex). The errors for masses obtained from Equations (6), (3), and (4) are the standard deviation of the residual distribution between the fitted masses and those of J. Huang et al. (2012, in preparation) (see Figure 1(c); $\sigma \approx 0.175$). Errors for $U-B$ and M_B obtained from

k-correct are estimated by measuring the 1σ dispersion from the *HST*/ACS V and I in the redshift range $0.64 < z < 0.68$ and $0.82 < z < 0.86$, respectively. Within these redshift ranges, rest-frame U and B approximately redshift into observed V and I, which, when combined with the high resolution of *HST*, gives us an accurate photometric error estimate. The average errors are ≈0.07 mag (U) and ≈0.05 mag (B). Errors for $U-B$ and M_B obtained from Equations (3) and (5) are taken to be the standard deviation between our fits and k-correct. For the mass–radius combinations, e.g., M_*/r_e, we propagate the errors from the masses and the GIM2D confidence limits.

3. SAMPLE SELECTION

Within the AEGIS region, ≈30,000 objects have both *HST*/ACS imaging and GIM2D decompositions; this is the master GIM2D sample. Only 11,223, however, have either a spectroscopic or photometric redshift (see Section 2). Moreover, although our redshift coverage is from $0.2 < z < 1.2$, in order to minimize k-corrections, we restrict our sample to $0.5 \leqslant z < 0.8$; this cuts our sample down to 3426, which will be referred to as the "starting" sample. To reduce the effects of dust, we only choose galaxies with axis ratios (b/a; as measured from the single n fit) greater than 0.55, further reducing our sample to 1567 galaxies.

Although GIM2D was run for every galaxy, not every decomposition is reliable. For example, galaxies with effective radii r_e less than half the FWHM of the PSF (2 pixels) are not well fit. Additionally, galaxy models created by GIM2D that are offset from the center of the *HST*/ACS image by more than 3.5 pixels are similarly ill fit. There are also instances where the fitting failed; eliminating these leaves us with 1427 objects. Note that we are only using the single Sérsic fit values for global galaxy parameters, and hence this sample consists of values only from the single n fit.

GIM2D was also used to produce measurements of every galaxy's bulge and disk through two different fits—the $n_{\rm bulge} = 4$ and $n_{\rm bulge} = 2$ decompositions, with the disk being $n = 1$ for both (see Section 2.3). Note that GIM2D bulge+disk decompositions do allow for a galaxy to have $B/T = 0$, i.e., a pure disk galaxy, if that is the optimal fit according to the Metropolis fitting algorithm (≈22% of the subcomponent sample have $B/T = 0$; see Simard et al. 2002 for more details). For each galaxy, we use the bulge+disk fit with the smallest χ^2. We only use the subcomponent measurements of the "final" sample, which we define below.

To reduce the effects of dust, we applied an axis ratio cut of $b/a > 0.55$. While this cut eliminates many edge-on dusty galaxies (Martin et al. 2007), it does not affect dusty face-on galaxies. To clean these from our sample, we calculate UVJ rest-frame magnitudes. The resultant $U-V$ versus $V-J$ two-color plot enables us to separate dusty red galaxies from truly quiescent red galaxies (Williams et al. 2009). We use the *Rainbow* software described in Barro et al. (2011a, 2011b). Briefly, the software applies a χ^2 minimization algorithm to find the best-fitting galaxy template from the multi-wavelength photometry of AEGIS. Then several filters (U Bessel, V Bessel, J Johnson) are convolved with the best template to estimate synthetic fluxes assuming a luminosity distance of 10 pc. Our results can be seen in the UVJ diagram (Figure 3). The upper-left region bounded by the solid lines within the UVJ diagram represents the quiescent region, as defined by Williams et al. (2009). Comparing the quiescent galaxies to the red sequence galaxies, which we define to be galaxies with $U - B > 1.20$ and are shown in red in Figure 3, shows excellent agreement; only 17[26] (6%) of the $U - B > 1.20$ galaxies lie outside the quiescent area. These are presumed to be dusty star formers and are discarded from our sample. There is an additional reduction of 8 $U - B > 1.20$ galaxies because we were unable to obtain their UVJ magnitudes. Since we do not know whether these galaxies are truly quiescent or simply dusty, we take the conservative route and discard them. To sum, we require our quiescent galaxies to have $U - B > 1.20$ *and* to lie within the quiescent region of the UVJ diagram. With this criterion, our galaxy sample has 1402 galaxies.

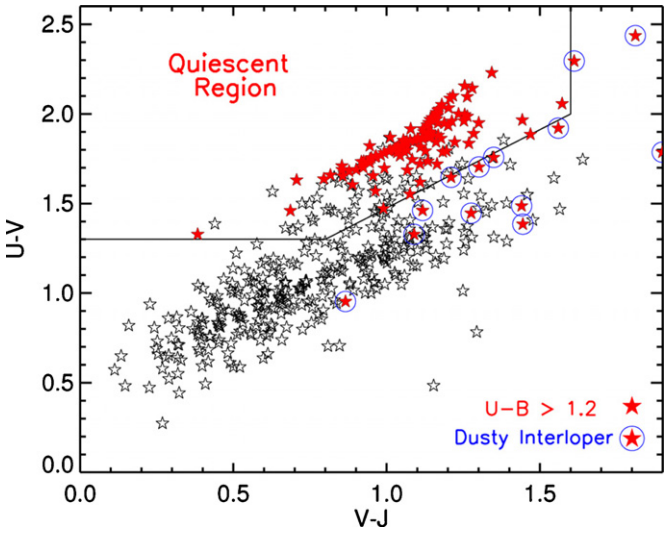

Figure 3. To address dust, we plot our sample in the rest-frame UVJ diagram. The quiescent population lies within the quiescent region as defined by Williams et al. (2009). Red points represent red sequence galaxies, defined to have $U - B > 1.20$. Almost all of the red sequence lies within the quiescent area. $U - B > 1.20$ galaxies outside the quiescent area are only ≈3% of the defined red sequence. These are the dusty star formers, and we eliminate them from the sample so that the red sequence galaxies are truly quiescent.

(A color version of this figure is available in the online journal.)

3.1. Completeness

Finally, we must discuss our sample's completeness. Because the DEEP2+3 spectroscopic survey is limited by an R-band magnitude of 24.1,[27] there is a selection bias against low-mass galaxies. Fortunately, the photometric sample goes deeper, down to an IRAC 3.6 μm flux of 2 μJy. Details of the photometric sample can be found in J. Huang et al. (2012, in preparation), but we will briefly summarize the key characteristics. The 3.6 μm selected sample spans the redshift range of $0.4 < z < 1.2$, where 3.6 μm also probes the rest-frame NIR (1.2–2.5 μm). Galaxies of all types have very similar SEDs in the NIR band. Therefore, a rest-frame NIR-selected sample suffers no bias against either blue or red galaxies (Cowie et al. 1996; Huang et al. 1997). Galaxy NIR luminosities also trace their underlying stellar mass; in other words, this sample is very close to a mass-selected sample. The K-band absolute magnitudes for galaxies in this sample are calculated with the 3.6 μm flux densities. The IRAC-to-K-band k-correction is adopted from De Propris et al. (2007). The absolute K-band magnitude range for this sample is $-19 < M_K < -25$. This translates into a limiting

[26] Four of these galaxies are not visible because they have UVJ magnitudes that are identical to those that are visible.

[27] There are some DEEP3 targets fainter than this limit (Cooper et al. 2011, 2012).

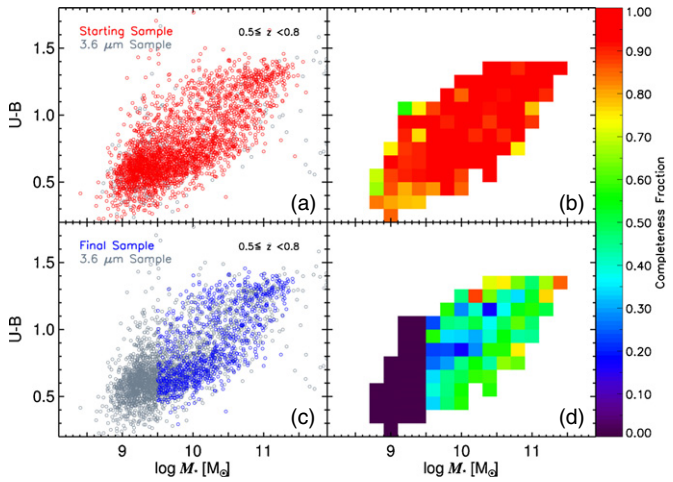

Figure 4. Left column: rest-frame $U-B$ vs. $\log M_*$ is plotted for the "starting" sample (red; top row) and the "final" sample (blue; bottom row). For comparison, the *Spitzer*/IRAC 3.6 μm selected sample (J. Huang et al. 2012, in preparation) in our redshift range $0.5 \leqslant z < 0.8$ is plotted in the background. Right column: $U-B$ vs. $\log M_*$ is binned with lengths in $U-B$ and $\log M_*$ that correspond roughly to their 1σ error; we only show bins with more than five galaxies. Within each bin, the fraction of the number of galaxies in that row's sample to that of the 3.6 μm selected sample is computed and displayed as the corresponding color indicated by the color bar to the right. The completeness of the "starting" sample is uniformly complete above $\log M_*/M_\odot = 9.5$. The completeness of the "final" sample is ~50% and is largely uniform. See the text for discussion.
(A color version of this figure is available in the online journal.)

stellar mass of $\log M_*/M_\odot = 9.5$. Therefore, cross-matching to the photometric sample has essentially eliminated the selection bias against low-mass galaxies of the DEEP2+3 surveys.

To illustrate our sample completeness, we compare the color–mass diagrams of our "starting" sample (red) to the *Spitzer*/IRAC 3.6 μm selected sample (gray) in Figure 4(a). There are hardly any gray points, indicating that the "starting" sample contains almost all the galaxies in the 3.6 μm selected sample. This is further illustrated in Figure 4(b), where we bin up the color–mass diagram with lengths in $U-B$ and $\log M_*$ that roughly correspond to their distributions' 1σ error; we only show bins with more than five galaxies. Within each bin, the fraction of the number of galaxies in the "starting" sample to that of the 3.6 μm selected sample is computed and displayed as the corresponding color indicated by the color bar to the right. Confirming what was seen in Figure 4(a), the completeness is almost perfect, and most importantly, the completeness is uniform, especially for $\log M_*/M_\odot > 9.5$, the mass limit of the 3.6 μm selected sample. Thus, our "starting" sample is uniformly complete down to the mass limit of the 3.6 μm selected sample.

However, our "starting" sample is not the ultimate sample we use. To get rid of bad data and dusty galaxies, we have imposed several requirements (see Section 3). To obtain our "final" sample, we impose one final requirement, $\log M_*/M_\odot > 9.5$. This last cut ensures that our "final" sample is complete above $\log M_*/M_\odot = 9.5$. Thus finally, we have our "final" sample, consisting of 943 galaxies. The "final" sample is what is plotted in all subsequent figures unless stated otherwise. The completeness of the "final" sample is illustrated in Figures 4(c) and (d). Figure 4(d) (calculates bins of completeness like in Figure 4(b)) shows that the completeness of the "final" sample is ~50%, with a dearth of galaxies on the top of the blue cloud, i.e., the green valley, and a surplus of galaxies on the upper red sequence. These features are due to the b/a criterion, which is meant to eliminate edge-on galaxies that are presumably dusty. Indeed, according to Martin et al. (2007), dusty galaxies do primarily reside on top of the blue cloud, which explains why there is a lack of galaxies on top of the blue cloud in the "final" sample compared to the 3.6 μm sample. The surplus of galaxies on top of the red sequence is also understandable since the reddest galaxies are elliptical galaxies that have intrinsically high axis ratios. Although there are some biases introduced into the "final" sample by these various cuts, we have tested the effects of removing them and find that it does not affect our conclusions. But we stress that these cuts are *necessary*; they remove bad data. Our "final" sample is a culmination of the best data from our available resources. For an extra discussion of our samples' surface brightness limits, data quality, and possible Sérsic index bias, please see Appendices A, B, and C.

All our data, including those that were not presented in this paper, are available online at http://people.ucsc.edu/~echeung1/data.html. Tables 1–5 present the key parameters we use in our paper for 20 randomly selected galaxies in our catalog. Table 1 presents basic information of our galaxies, including their unique IDs, derived photometric quantities, and stellar masses from both k-correct and Equations (6), (3), and (4). Table 2 presents much of the same information in Table 1, but only for the subcomponents. Tables 3, 4, and 5 present the three GIM2D catalogs: the single Sérsic fit, $n_{\rm bulge} = 4$ fit, and $n_{\rm bulge} = 2$ fit, respectively. These GIM2D catalogs provide many measurements, including V, I, and r_e for both the galaxy and its subcomponents. The rest of the measurements and galaxies can be obtained online.

Table 2
Subcomponent Properties

DEEPID	M_B Bulge	M_B Disk	$U-B$ Bulge	$U-B$ Disk	M_* Bulge	M_* Disk
(1)	(2)	(3)	(4)	(5)	(6)	(7)
13049654	−15.95	−17.22	1.15	0.73	8.99	9.02
13018599	−19.17	−19.64	1.53	1.05	10.27	10.12
12020067	−18.85	−18.68	0.73	0.61	9.39	9.14
12007757	−20.30	−20.55	1.00	0.66	10.18	9.63
13040619	−19.62	−19.88	1.07	1.52	10.11	10.57
13048556	−19.15	−19.52	0.54	0.66	9.13	9.49
13049852	−19.33	−20.34	1.34	1.42	10.23	10.70
13026131	−17.65	−18.11	1.24	0.74	9.48	9.07
12020067	−18.85	−18.68	0.73	0.61	9.39	9.14
12015606	−19.84	−20.20	1.20	0.60	10.33	9.66
13058131	−19.60	−20.08	1.50	1.06	10.45	10.29
12016156	−18.85	−18.91	0.67	0.41	9.25	8.79
13012297	−21.05	−19.37	1.25	1.18	10.89	10.16
12007918	−19.91	−19.75	1.01	0.50	10.15	9.29
13011795	−18.66	−18.93	1.37	1.18	10.00	9.96
13064645	−21.00	−21.29	0.75	0.88	10.63	10.96
12016799	−20.27	−19.62	1.31	0.97	10.59	9.98
12023870	−18.35	−17.82	0.71	0.47	9.14	8.51
12004470	−18.40	−18.64	0.64	0.48	9.07	8.86
12020439	−18.26	−18.41	0.95	0.52	9.41	8.81

Notes. The same 20 randomly selected galaxies from Table 1 are shown. The entire catalog is available at http://people.ucsc.edu/~echeung1/data.html. Column 1: unique DEEPID. Column 2: absolute B-band magnitude of bulge derived from Equations (3) and (4). Column 3: absolute B-band magnitude of disk derived from Equations (3) and (4). Column 4: $U-B$ rest-frame color of bulge derived from Equation (5). Column 5: $U-B$ rest-frame color of disk derived from Equation (5). Column 6: M_* of bulge derived from Equations (3) and (6). Column 7: M_* of disk derived from Equations (3) and (6).

Table 3
GIM2D: Single *n* Catalog

DEEPID	*V*	*I*	*n*	*e*	r_e (pixels)	χ^2 *V* band	χ^2 *I* band
(1)	(2)	(3)	(4)	(5)	(6)	(7)	(8)
13049654	22.07	21.56	1.11	0.68	18.31	1.16	1.07
13018599	24.17	22.70	1.36	0.62	15.54	1.05	1.16
12020067	22.46	21.96	1.70	0.43	10.71	1.13	1.05
12007757	23.73	22.84	1.17	0.58	23.76	1.09	1.03
13040619	22.89	21.42	6.00	0.13	19.63	1.04	0.92
13048556	22.28	21.75	4.16	0.66	78.14	1.05	0.93
13049852	21.80	20.41	4.79	0.23	27.88	1.00	1.12
13026131	23.95	23.12	1.09	0.53	15.39	0.97	0.95
12020067	22.46	21.96	1.70	0.43	10.71	1.13	1.05
12015606	22.48	21.54	1.59	0.03	15.41	1.08	0.98
13058131	22.95	21.36	5.07	0.29	34.61	1.01	0.92
12016156	23.85	23.23	1.40	0.49	29.93	1.12	0.99
13012297	23.31	21.67	2.82	0.15	13.04	0.89	0.82
12007918	22.65	21.97	1.63	0.41	10.73	1.18	1.10
13011795	24.10	22.51	5.94	0.30	16.12	0.88	0.81
13064645	23.97	22.49	5.99	0.25	12.85	0.96	0.93
12016799	23.02	21.76	1.36	0.46	21.21	1.15	1.09
12023870	23.13	22.70	4.64	0.46	8.98	1.21	1.18
12004470	22.71	22.34	1.66	0.41	5.67	1.62	1.48
12020439	23.69	23.09	1.32	0.68	6.24	1.10	1.15

Notes. The same 20 randomly selected galaxies from Table 1 are shown. The entire catalog is available at http://people.ucsc.edu/~echeung1/data.html. Every value in this table is from the GIM2D decomposition that only fits for a single Sérsic index. These are the primary data we use throughout this paper, including the basic *V* and *I* of the galaxy. Column 1: DEEPID. Column 2: *V*-band magnitude of galaxy. Column 3: *I*-band magnitude of galaxy. Column 4: Sérsic index of galaxy. Column 5: ellipticity of galaxy ($e \equiv 1 - b/a, b \equiv$ semi-minor axis, $a \equiv$ semi-major axis). Column 6: effective radius of the galaxy measured along the major axis in units of pixels. Column 7: χ^2 of fit in the *V* band. Column 8: χ^2 of fit in the *I* band.

4. RESULTS

4.1. The Most Discriminating Color Parameter

We begin by intercomparing the various *global* structural parameters discussed in the introduction to find which is the best predictor of color. Figure 5 plots $U - B$ rest-frame color against six quantities for the final galaxy sample: rest-frame absolute *B*-band magnitude M_B, stellar mass M_*, stellar mass divided by semimajor axis effective radius M_*/r_e (sometimes called the "inferred velocity dispersion"),[28] M_*/r_e^2 (nominal surface density),[29] Sérsic index *n*, and inner stellar mass surface density $\Sigma^*_{1\,\mathrm{kpc}}$ (we defer discussion of $\Sigma^*_{1\,\mathrm{kpc}}$ to Section 4.3.3). The 1σ error bars are given in the top right of each panel (see Section 2.8 for details). The spectroscopic sample and photometric sample are shown by open stars and open circles, respectively; we use this scheme throughout the rest of the paper. As stated in the introduction, the amount of color overlap is one measure of how well a parameter separates red sequence and blue cloud galaxies, and parameters that reduce this overlap are better discriminators of galaxy quenching. The sample considered is the "final" sample, which is complete only in stellar mass, as defined in Section 3. Thus, the results of the following analysis are only applicable for the "final" sample. The goal of this section is to quantify the amount of overlap in order to determine the single best color discriminant among the traditional parameters.

As in Strateva et al. (2001), the color–magnitude diagram (Figure 5(a)) shows a clear red sequence and blue cloud. However, these two groups overlap greatly over the entire range of absolute magnitude. This confirms the well-known result that the *B*-band magnitude is a poor predictor of galaxy color.

Figure 5(b) shows the color–mass diagram. As shown by Kauffmann et al. (2003) and Borch et al. (2006), mass is better correlated with star formation history than is luminosity. Although the relationship with color is improved, the range of color overlap is still large, extending over ~0.8 dex in mass. Figures 5(c) and (d) add powers of r_e in the denominator to M_*, in the form of M_*/r_e^p. The smallest overlap by eye is given by M_*/r_e in Figure 5(c), while mass surface density M_*/r_e^2 in Figure 5(d) looks slightly worse. Thus, this new DEEP2 sample indicates that M_*/r_e is a superior color discriminator to surface mass density M_*/r_e^2.

To summarize, effective radius r_e tightens the basic color–mass relation because red galaxies at fixed mass are smaller than blue galaxies, and the tightest correlation is obtained using M_*/r_e.

We plot in Figure 5(e) color versus Sérsic index *n*. The character of this plot is markedly different from the others—rather than a smooth trend with color within the blue cloud as in, for example, M_*/r_e, the color jump is more abrupt, with color remaining constant above and below what appears to be a critical value of *n* around $\log n = 0.36$ ($n = 2.3$). This behavior is intriguing because it might signal a *real physical threshold* in Sérsic index, above which star formation shuts down. As stated in the introduction, *n* likely plays an important role in quenching star formation. Blanton et al. (2003) and Schiminovich et al. (2007) demonstrated a trend between *n* and color for SDSS galaxies. Driver et al. (2006) and Allen et al. (2006) also showed this relationship with their Millennium catalog. And Wuyts et al. (2011) demonstrated that this relationship persists out to $z \sim 2.5$. Bell (2008) and Bell et al. (2012) explored this correlation and showed that high *n* is necessary for quenching but not sufficient—there are many galaxies that are blue despite having high *n*. We see something similar in our data with the scattering of aberrant points in the lower-right-hand corner of Figure 5(e). We term these aberrant points "outliers" and discuss them further in Section 4.3.2.

The above conclusions are based mainly on visual assessment of Figure 5. To quantify our results, we now present two new quantities that are designed to measure the size of the overlap regions. These measurements can be applied to rank the predictive power of the various structural parameters and also to identify galaxies within the overlap regions for further study. To define these quantities, we first bin the sample by the parameter of interest. Then, within each bin, we find the fraction of galaxies that are red, i.e., galaxies with $U - B > 1.20$, which we have ensured to be genuinely quiescent and not dusty (see Section 3). The locations where this fraction equals 15% and 60% mark the beginning and end of the overlap region, respectively; these percentages were adjusted to match the core of the overlap regions as judged by eye and are a compromise over all diagrams. We varied the overlap definition with various permutations of starting boundaries in the red fraction range of

[28] The true stellar velocity dispersion is $\sigma^2 \propto GM/r_e$, where *M* is the total mass including stars, gas, and dark matter. Franx et al. (2008) provide a value of the coefficient through the fitting of a sample of SDSS galaxies: $\sigma^2 = 0.3GM_*/r_e$. Recently, Taylor et al. (2010) and Bezanson et al. (2011) showed that the addition of a Sérsic-dependent term to the "inferred velocity dispersion" of Franx et al. (2008) provides a better estimate of the true velocity dispersion. We choose not to use this updated "inferred velocity dispersion" because we want to compare the color correlations of these parameters independently.

[29] Surface mass density is actually $M_*/2\pi r_e^2$, but we omit the constants.

Table 4
GIM2D: $n = 4$ Bulge Catalog

DEEPID	V Bulge	V Disk	I Bulge	I Disk	B/T	B/T	r_e Bulge	r_d Disk	C	C	χ^2	χ^2
					V Band	I Band	(pixels)	(pixels)	V Band	I Band	V Band	I Band
(1)	(2)	(3)	(4)	(5)	(6)	(7)	(8)	(9)	(10)	(11)	(12)	(13)
13049654	22.83	22.42	22.07	22.00	0.41	0.48	33.36	11.54	0.47	0.47	1.11	1.01
13018599	27.39	24.32	29.81	22.78	0.06	0.00	3.27	8.56	0.48	0.58	1.08	1.20
12020067	23.22	23.07	22.47	22.71	0.46	0.56	19.41	5.88	0.55	0.58	1.13	1.05
12007757	25.53	23.82	23.91	23.15	0.17	0.33	19.84	17.86	0.35	0.36	1.06	1.02
13040619	24.11	24.14	22.87	22.28	0.51	0.37	2.78	9.96	0.62	0.69	1.01	0.89
13048556	23.57	23.30	23.10	22.68	0.44	0.41	23.76	29.41	0.49	0.45	1.01	0.89
13049852	23.30	22.53	21.96	21.10	0.33	0.31	3.73	16.14	0.61	0.64	0.93	0.89
13026131	26.47	24.05	25.78	23.21	0.10	0.09	7.93	9.66	0.41	0.46	0.97	0.96
12020067	23.22	23.07	22.47	22.71	0.46	0.56	19.41	5.88	0.55	0.58	1.13	1.05
12015606	24.46	22.67	22.88	21.95	0.16	0.30	11.22	10.18	0.48	0.44	1.08	0.97
13058131	24.43	23.65	22.59	22.42	0.33	0.46	7.95	19.11	0.57	0.55	0.97	0.88
12016156	28.30	23.97	25.40	23.57	0.02	0.16	18.57	15.65	0.40	0.30	1.11	1.00
13012297	23.47	25.07	21.80	23.52	0.81	0.83	16.04	6.93	0.55	0.58	0.89	0.82
12007918	23.45	23.19	22.35	22.74	0.44	0.59	19.23	5.87	0.55	0.56	1.16	1.07
13011795	24.78	25.27	23.12	24.09	0.61	0.71	6.49	12.72	0.66	0.65	0.87	0.81
13064645	24.95	25.15	23.56	23.36	0.55	0.45	2.26	10.60	0.69	0.71	0.94	0.88
12016799	30.56	23.11	28.18	21.85	0.00	0.00	13.39	11.62	0.36	0.38	1.17	1.14
12023870	23.39	24.42	22.83	24.18	0.72	0.78	21.91	1.89	0.66	0.71	1.14	1.15
12004470	23.32	23.27	22.90	22.94	0.49	0.51	11.73	3.03	0.73	0.74	1.53	1.42
12020439	24.77	24.01	23.65	23.61	0.33	0.49	13.89	3.54	0.65	0.72	1.02	1.06

Notes. The same 20 randomly selected galaxies from Table 1 are shown. The entire catalog is available at http://people.ucsc.edu/~echeung1/data.html. Every value in this table is from the GIM2D decomposition using a bulge and disk with Sérsic index of $n = 4$ and $n = 1$, respectively. Column 1: DEEPID. Columns 2 and 3: V-band magnitude of bulge and disk. Columns 4 and 5: I-band magnitude of bulge and disk. Column 6: B/T in the V band. Column 7: B/T in the I band. Column 8: effective radius of major axis of bulge in units of pixels. Column 9: scale length of disk measured along major axis in units of pixels. Column 10: concentration with $\alpha = 0.3$ in V. Column 11: concentration with $\alpha = 0.3$ in I. Column 12: Chi-squared of fit in V. Column 13: Chi-squared of fit in I.

Table 5
GIM2D: $n = 2$ Bulge Catalog

DEEPID	V Bulge	I Bulge	V Disk	I Disk	B/T	B/T	r_e Bulge	r_e Disk	C	C	χ^2	χ^2
					V Band	I Band	(pixels)	(pixels)	V Band	I Band	V Band	I Band
(1)	(2)	(3)	(4)	(5)	(6)	(7)	(8)	(9)	(10)	(11)	(12)	(13)
13049654	23.33	22.38	22.51	21.90	0.29	0.36	24.61	10.97	0.47	0.47	1.11	1.00
13018599	25.53	24.55	23.41	23.23	0.29	0.46	20.65	8.46	0.48	0.58	1.05	1.12
12020067	23.02	23.16	22.43	22.70	0.53	0.56	23.38	4.43	0.53	0.55	1.05	0.98
12007757	24.66	23.79	23.48	23.18	0.31	0.43	14.76	35.53	0.35	0.36	1.04	0.98
13040619	24.40	23.95	23.20	22.18	0.40	0.28	1.92	9.09	0.62	0.69	1.01	0.90
13048556	22.99	25.33	22.59	23.80	0.90	0.75	28.14	30.87	0.50	0.48	1.11	0.96
13049852	23.48	22.48	22.14	21.05	0.28	0.27	3.13	15.79	0.61	0.64	0.93	0.88
13026131	24.93	24.34	23.73	23.68	0.37	0.49	19.07	9.98	0.41	0.46	0.95	0.93
12020067	23.02	23.16	22.43	22.70	0.53	0.56	23.38	4.43	0.53	0.55	1.05	0.98
12015606	23.71	22.89	22.36	22.30	0.32	0.49	10.64	11.16	0.48	0.44	1.07	0.97
13058131	24.81	23.55	22.95	22.23	0.24	0.34	4.94	17.80	0.57	0.55	0.97	0.88
12016156	24.67	24.31	23.93	23.91	0.42	0.49	27.86	30.96	0.40	0.30	1.11	0.96
13012297	23.44	−99.99	21.80	−99.99	1.00	1.00	10.84	6.88	0.55	0.58	0.91	0.88
12007918	23.33	23.54	22.77	22.68	0.55	0.48	9.21	7.01	0.55	0.56	1.17	1.08
13011795	25.30	24.90	23.63	23.50	0.41	0.47	3.11	13.02	0.66	0.65	0.87	0.80
13064645	25.29	24.90	23.93	23.21	0.41	0.34	1.36	8.69	0.69	0.71	0.94	0.89
12016799	23.41	23.85	21.90	22.78	0.60	0.69	44.45	9.40	0.36	0.38	1.11	1.06
12023870	23.71	24.13	23.12	23.82	0.60	0.66	21.50	1.75	0.66	0.71	1.14	1.15
12004470	23.50	23.19	23.00	22.89	0.43	0.47	14.01	2.61	0.73	0.74	1.48	1.37
12020439	24.56	24.16	23.63	23.72	0.41	0.52	12.21	3.11	0.65	0.72	0.98	1.05

Notes. The same 20 randomly selected galaxies from Table 1 are shown. The entire catalog is available at http://people.ucsc.edu/~echeung1/data.html. Every value in this table is from the GIM2D decomposition using a bulge and disk with Sérsic index of $n = 2$ and $n = 1$, respectively. Column 1: DEEPID. Columns 2 and 3: V-band magnitude of bulge and disk. Columns 4 and 5: I-band magnitude of bulge and disk. Column 6: B/T in the V band. Column 7: B/T in the I band. Column 8: effective radius of major axis of bulge in units of pixels. Column 9: scale length of disk measured along major axis in units of pixels. Column 10: Concentration with $\alpha = 0.3$ in V. Column 11: concentration with $\alpha = 0.3$ in I. Column 12: Chi-squared of fit in V. Column 13: Chi-squared of fit in I.

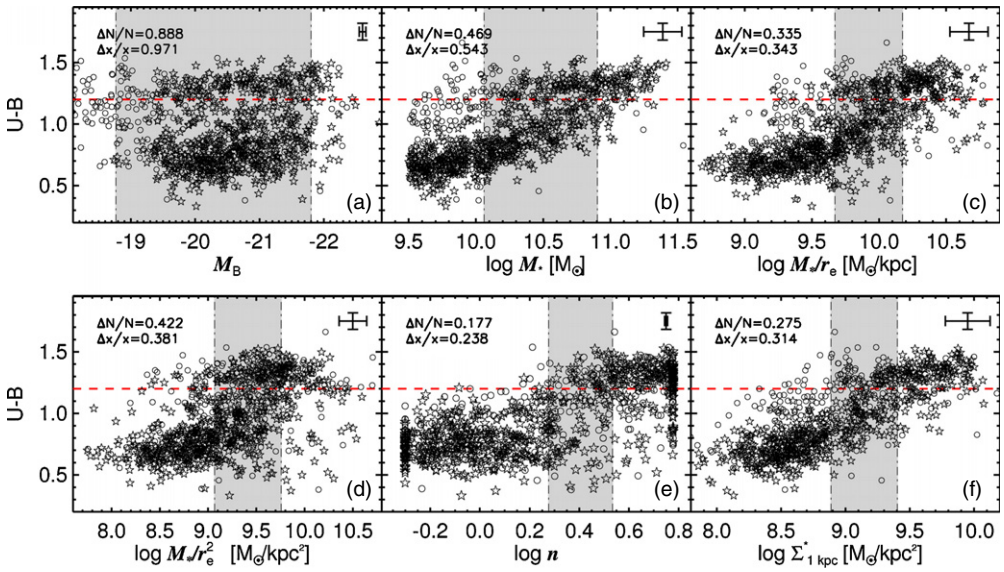

Figure 5. Rest-frame $U-B$ color is plotted against (a) rest-frame absolute B-band magnitude M_B, (b) stellar mass M_*, (c) stellar mass divided by semimajor axis effective radius M_*/r_e, (d) M_*/r_e^2 (surface density), (e) Sérsic index n, and (f) stellar mass surface density within 1 kpc $\Sigma^*_{1\,\mathrm{kpc}}$. M_* is in solar masses and r_e is in kpc. The stars and circles represent galaxies with spectroscopic redshifts and photometric redshifts, respectively. 1σ error bars are displayed in the upper right of each panel. The overlap region of each parameter is highlighted in gray. Overlap regions are defined as regions in which the fraction of red galaxies is between 15% and 60% (see Section 4.1). The red horizontal line represents the division between red and blue galaxies. The top left corner of each panel shows two measures of the size of the overlap region: the fractional number of galaxies within the overlap region $\Delta N/N$ and the fractional extent of the region $\Delta x/x$, where x contains 90% of the points (see the text). This analysis was done on the "final" sample, which is complete only in stellar mass (down to $\log M_*/M_\odot = 9.5$; see Section 3.1). By both measures, M_*/r_e outperforms other parameters of the form M_*/r_e^p, which we have confirmed by studying intermediate values of p. Sérsic index and $\Sigma^*_{1\,\mathrm{kpc}}$ do even better, hinting that the distribution of mass in the inner parts of galaxies may play a fundamental role in quenching star formation.

(A color version of this figure is available in the online journal.)

5% to 20% and ending boundaries from 40% to 60% and found that the results are unchanged. To find the locations of the edges of the overlap regions, we fit a fourth-order polynomial to the red fraction bins and interpolate to find where the fit reaches the desired fractions. Each parameter has been divided into 25 bins, and each edge value is examined to ensure that the choice is sensible. The edge locations depend only weakly on the choice of bin width—for example, in the case of M_*/r_e, bin sizes in the range 0.07–0.25 dex produce similar results.

We define two measures to quantify the sizes of the overlap regions. The first is the fractional number of galaxies in the region, $\Delta N/N$, where N is the total number of galaxies and ΔN is the number within the overlap region. The second is the fractional extent of the region, $\Delta x/x$, where Δx is the width of the overlap and x is the range that includes 90% of the data (excluding 5% at either end). The resulting overlap regions for each parameter are demarcated in gray in Figure 5, and the upper left corner of each panel shows the two measures $\Delta N/N$ and $\Delta x/x$. These quantitative measures confirm what was seen by eye, namely, that M_*/r_e gives the smallest values of both $\Delta N/N$ and $\Delta x/x$ among all the mass–radius combinations. Note that the relative extent of M_B is $\Delta x/x = 0.971$; this simply means that the overlap region is almost equal to the entire range that encompasses 90% of the data, again agreeing with our previous qualitative assessment. Furthermore, we find that Sérsic index performs considerably better than even M_*/r_e in minimizing both $\Delta N/N$ and $\Delta x/x$.

We also point out the extremely tight relation that is produced when plotting color versus M_*/r_e or M_* *for blue-cloud galaxies alone* (Figures 5(b) and (c)). This has been pointed out before and is referred to as the "main sequence" of star formation (Noeske et al. 2007). Previous work on quenching has focused on the relationship between red sequence and blue cloud galaxies and not so much on the properties of galaxies within the blue cloud itself. However, the tightness of the relation between M_*/r_e (or M_*) and color for star-forming galaxies alone could be an important clue to the physics of quenching, and we return to this point in Section 5.

4.2. Properties of Galaxies in the M_*/r_e Overlap Region

We have shown that our AEGIS data duplicate previous findings showing that M_*/r_e and n correlate strongly with quenching, but we have also shown that neither parameter alone is close to being a perfect predictor of it. In this section and the next, we take a further look at the properties of galaxies in the overlap region and outliers to find out whether multiple parameters can be used in concert to predict quenching, and whether this interplay sheds light on the physical processes involved.

Figure 6 investigates residual trends within the M_*/r_e overlap region of Figure 5(c) by plotting color versus various structural parameters for overlap galaxies alone. In exploring this slice of M_*/r_e, we are assuming a general evolutionary sequence such that the blue galaxies evolve into the red galaxies within this overlap region. However, this assumption is not without proof. Bell et al. (2004b) and Faber et al. (2007) have shown that the red sequence has increased by ∼2 while the blue cloud has remained relatively stable from $z \sim 1$ to $z = 0$. Moreover, Hopkins et al. (2010b) showed that ∼65%–80% of the observed mass density of bulge-dominated galaxies formed since $z \sim 1$. Thus, our redshift range ($0.5 \leqslant z < 0.8$) peers directly into the epoch when the majority of red sequence galaxies are being formed. We choose M_*/r_e as the base parameter because it is the tightest M_*–r_e combination in Figure 5, but similar results are obtained when M_* is used.

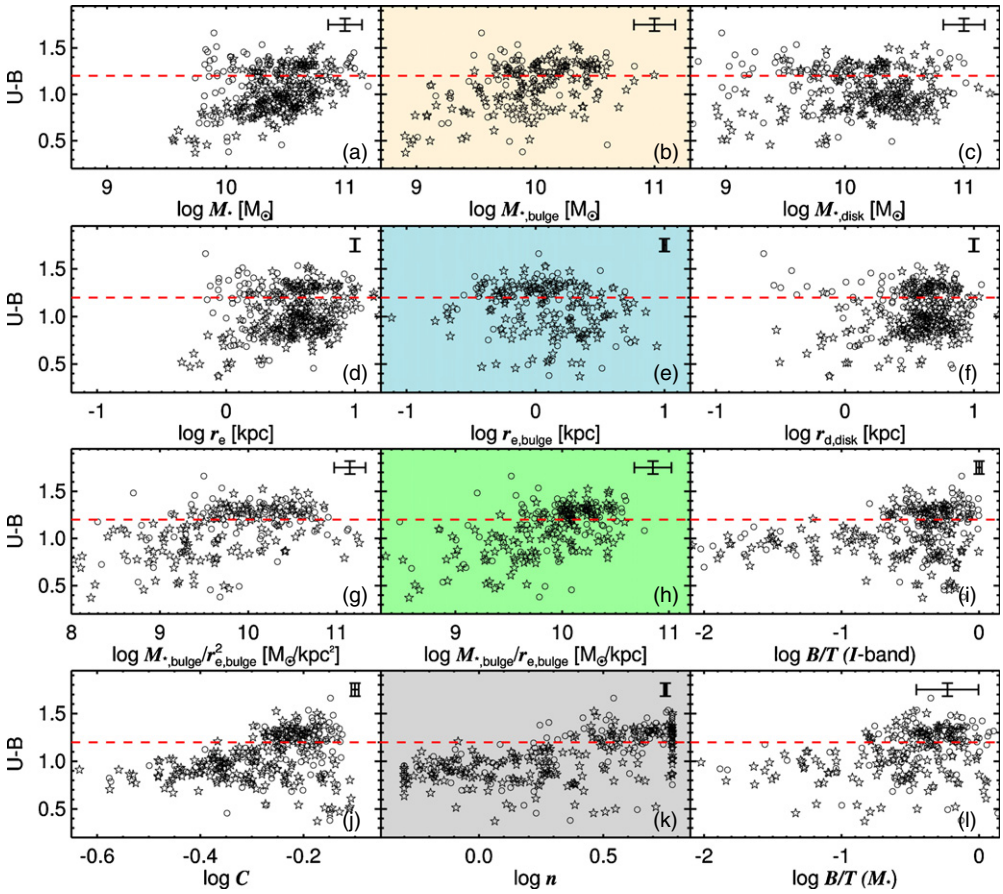

Figure 6. Galaxies in the overlap region of $M_*/r_{\rm e}$ (containing 316 galaxies) from Figure 5(c) are isolated to examine possible second-parameter color correlations with both global and disk/bulge properties. $U-B$ rest-frame color is plotted against (a) global stellar mass M_*, (b) bulge stellar mass $M_{*,\rm bulge}$, (c) disk stellar mass $M_{*,\rm disk}$, (d) global semimajor axis effective radius $r_{\rm e}$, (e) bulge semimajor axis effective radius $r_{\rm e,bulge}$, (f) disk semimajor axis exponential scale length $r_{\rm d,disk}$, (g) $M_{*,\rm bulge}/r^2_{\rm e,bulge}$, (h) $M_{*,\rm bulge}/r_{\rm e,bulge}$, (i) bulge-to-total ratio B/T in the I band, (j) concentration C, (k) global Sérsic index n, and (l) B/T based on stellar mass M_*. The 1σ error bars are displayed in the upper right of each panel. The red horizontal line in each panel represents the division between red and blue galaxies. Global properties hardly differ between red and blue galaxies (white panels), but bulge properties, disk scale length, and n show key differences (colored panels and panel (c)). Specifically, red sequence bulges are physically smaller, yet more massive, than those of the blue cloud. Moreover, red sequence disks are less massive than their blue cloud counterparts. These trends cannot be produced by simple disk fading but require a concentration of inner stellar mass.

(A color version of this figure is available in the online journal.)

Panels (a), (d), (j), and (k) of Figure 6 plot integrated quantities, while the remaining panels introduce structural parameters (e.g., M_* and $r_{\rm e}$) for bulges and disks separately. Among the integrated properties, virtually no trend is seen in either stellar mass (panel (a)) or $r_{\rm e}$ (panel (d)), but a mild "step function" is seen with Sérsic index in that n is significantly higher for quenched galaxies (panel (k), gray). Concentration, C, shows similar behavior, albeit less cleanly (panel (j)). A similar trend with n was seen for *all* galaxies (Figure 5(e)), but it is important to see the same effect for overlap galaxies alone. This establishes beyond doubt that $M_*/r_{\rm e}$ alone does not fully encapsulate the processes needed to quench star formation. A possible interpretation is that some galaxies are "ripe" for quenching based on $M_*/r_{\rm e}$ and that a second process, which drives galaxies to high n, ultimately quenches star formation. We return to this idea later in Section 5.

The remaining panels in Figure 6 focus on the properties of bulge and disk components separately (the subcomponent sample; see Section 2.3). These parameters are derived from GIM2D photometric fits and M_*/L_B values from the $V-I$ colors of bulges and disks separately (Section 2.7), for which high-resolution two-color *HST* imaging is required. The striking result from the subcomponent panels in Figure 6 is the marked differences in *disk* mass, *bulge* mass, and *bulge* effective radius between blue and red overlap galaxies (panels (b), (c), and (e)). The disks of red sequence galaxies are less massive by about 0.2 dex than the blue cloud galaxies (panel (c)), while the bulges of red sequence galaxies are more massive by about 0.3 dex than the blue cloud galaxies (panel (b), in light tan). At the same time, disk sizes remain constant but bulge sizes decrease by about 0.3 dex as blue cloud galaxies transition to the red sequence (panel (e), in blue). These differences between red sequence bulges and blue cloud bulges amount to a difference of 0.6 dex in bulge $M_{*,\rm bulge}/r_{\rm e,bulge}$ (panel (h), in green). A similar trend is seen in B/T ratios, but it is weaker due to the large spread of blue galaxies.

These trends collectively demonstrate a real structural difference between the *inner stellar mass distributions* of quenched versus star-forming galaxies, and furthermore that this difference exists even within a narrow range of $M_*/r_{\rm e}$. Higher central stellar mass densities in quenched galaxies have been inferred in previous work from higher integrated Sérsic values (Weiner et al. 2005; Bundy et al. 2010), but photometric data by themselves do not rule out a simple fading picture in which disks decline in brightness, permitting an underlying high-n bulge to emerge. Actual stellar masses for bulges and disks separately

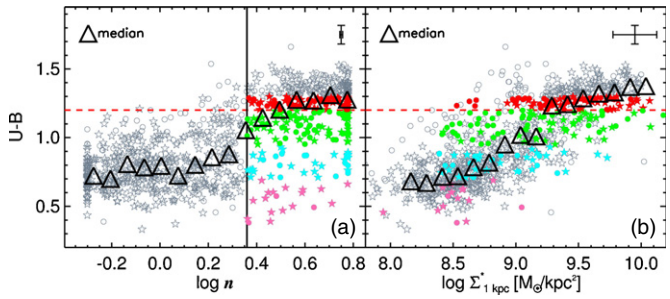

Figure 7. (a) The $U-B$ vs. n diagram is reproduced from Figure 5(e) with median values of color in each n bin plotted as open black triangles. The red horizontal line represents the division between red and blue galaxies, while the black vertical solid line at $\log n = 0.36$ represents the point at which the median is halfway between the red and blue values. The medians show a step-like behavior in $U-B$ vs. n, suggestive of a physical threshold in n. Exceptions to the step function are the blue "outlier" galaxies in the lower right. These are highlighted in strips of color for further discussion in Section 4.3.2 and Figure 9: pink points encompass $U-B < 0.70$, cyan points encompass $0.70 \leqslant U-B < 0.95$, and green points encompass $0.95 \leqslant U-B < 1.20$. Bluish red-sequence galaxies are highlighted for comparison and lie within $1.20 \leqslant U-B < 1.30$. Images of these outliers are shown in Figure 9. Roughly 40% of the $\log n > 0.36$ galaxies are outliers. (b) $U-B$ color vs. inner stellar mass surface density $\Sigma^*_{1\,\mathrm{kpc}}$. Note that some galaxies do not have $\Sigma^*_{1\,\mathrm{kpc}}$ measurements due to insufficient S/N. Most outliers now fall into line, suggesting that inner stellar mass surface density is a cleaner predictor of quenching than n.

(A color version of this figure is available in the online journal.)

are needed to rule out fading. An important new insight from our work is that evolution to the red sequence appears to be accompanied by a *significant rearrangement of inner stellar mass* in which existing stars move to the centers of galaxies, and/or new stars are formed there. We discuss processes whereby that might happen in Section 5.

4.3. Sérsic Index and Inner Surface Density

4.3.1. A threshold in n?

The previous section considered M_*/r_e as the main quenching parameter and looked at scatter around it to discover secondary effects. In this section, we use a similar tack but focus on Sérsic index n. An enlarged version of the color-n plot is shown in Figure 7(a), which indicates median $U-B$ in bins of n. The medians illustrate the striking step-like behavior previously mentioned. Defining the riser of the step to be where the medians are halfway between their red and blue values, we place this point at $\log n = 0.36$, which is marked with the vertical black line. This value corresponds to $n = 2.3$, which is similar to the value of n often used to distinguish quenched (or early-type) galaxies from star-forming ones locally (e.g., Shen et al. 2003; Bell et al. 2004a; Schiminovich et al. 2007; Drory & Fisher 2007).

The medians also emphasize how *flat* the color trends are above and below the threshold n value. Evidently, in the extreme high-n and low-n regimes, star formation history is independent of n. This differs markedly from the behavior of M_*/r_e; Figure 5(c) shows a strong correlation between M_*/r_e and color for star-forming galaxies *below* the overlap region.

The lack of importance of n above and below the threshold is further emphasized by the large color scatter in both of these regimes. This scatter is, however, of two types. At low n, there is a rather uniform spread in color, i.e., SSFR can assume any value within a large range, and n does not predict what SSFR will be. At high n, n predicts color much better, i.e., the color distribution is strongly peaked toward red (quenched) colors, but a significant tail of outliers with blue colors exists (colored points, except the red in Figure 7). The existence of these outliers was seen at both low and high redshifts by Bell (2008) and Bell et al. (2012), who expressed the role of n in quenching as "necessary but not sufficient," i.e., all quenched galaxies have high n, but not all high-n galaxies are quenched. We see the same thing.

Unlike Figure 5(c) (which plotted color versus M_*/r_e), there is no interval in n where the color scatter is markedly larger than elsewhere (Figure 7(a)), and thus no impetus to search for a second parameter within a *narrow region* of n. To investigate the scatter, we have replotted Figure 7, this time highlighting galaxies within narrow bins of various second parameters. The results are shown in Figure 8, where galaxies are divided into bins of stellar mass (top row), M_*/r_e (middle row), and M_*/r_e^2 (bottom row), collectively termed M_*/r_e^p. The outlier region from Figure 7(a) is outlined in blue. In each row, the behavior is the same. Galaxies with low values of M_*/r_e^p are seen to be mainly blue. A few leak into the high-n "outlier" regime, but their blue colors always agree with other galaxies in the same parameter bin, i.e., their star formation rates are not depressed by having high n. As M_*/r_e^p increases, the mean color of low-n galaxies becomes redder while the number of outliers remains relatively constant. Again, the colors of the outliers still agree with the average color of all galaxies in the same M_*/r_e^p bin. At the highest values of M_*/r_e^p, virtually all galaxies are quenched and the fraction of outliers is negligible. Two points are clear: dividing galaxies into bins has not destroyed the basic step-like nature of the behavior in that galaxies within each bin still trend smoothly but sharply (apart from outliers) from their "native" star-forming state to a quenched state. The second point is that all trends with color at low n remain flat within each bin of M_*/r_e^p. This shows that the strong trend of color versus M_* or M_*/r_e within the blue cloud (Figures 5(b) and (c)) is not caused by some hidden dependence on n.

To summarize, we have reproduced findings by previous authors that indicate that high n typically predicts a quenched galaxy, and we have set the half-power point between blue and red galaxies at $n_{\mathrm{crit}} = 2.3$. This value is very near the SDSS value, implying no large evolution in n_{crit} from $z \sim 0.65$ down to $z \sim 0$. The rise in color near the critical value is sharp, while above and below this value there is no trend in color with n, even within narrow slices of M_*/r_e^p. At high n, most galaxies are quenched with red colors, but a non-negligible fraction of objects is blue despite having high n. We turn to the nature of these outliers next.

4.3.2. Outliers

Although n acts like a threshold for the vast majority of galaxies, there are obvious exceptions, namely, the blue, high-n ($\log n \geqslant 0.36$) "outliers" highlighted in Figure 7(a) and elsewhere. Understanding these objects is clearly crucial for unraveling the quenching mechanism—why are they blue when their photometric structure resembles that of quenched objects? We have highlighted 151 outliers in Figure 7 using color to indicate their $U-B$ ranges; they make up ≈40% of all $n > 2.3$ galaxies (the red points immediately above the red horizontal dashed line at $U-B = 1.20$ are not outliers; they are quiescent red sequence galaxies shown for comparison).

Several possibilities come to mind to explain these objects. One possibility is that they are artifacts due to the presence of bright point-like AGNs. Adding a blue AGN to a normal star-forming galaxy would make the global colors bluer and increase n (and concentration) (Pierce et al. 2010). To pursue this, we

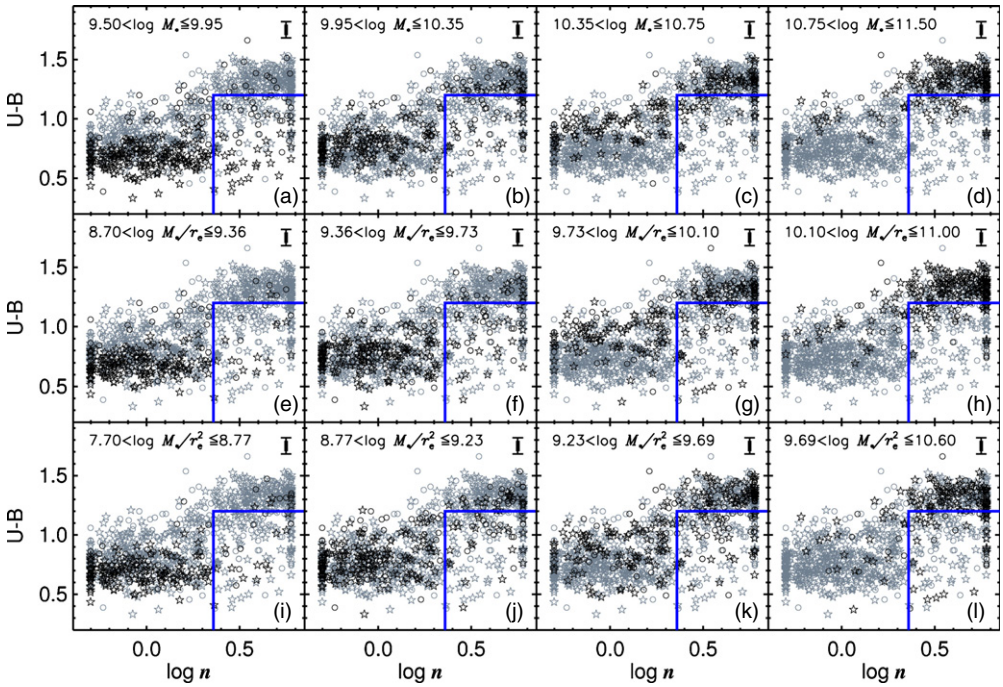

Figure 8. $U-B$ vs. n diagram from Figure 7(a) is replotted to separate the roles of M_*, M_*/r_e, and M_*/r_e^2 from n in driving color evolution. Galaxies are divided into bins of M_*/r_e^p and plotted as the black points. Bin boundaries are shown in the upper left of each panel. The rectangles outlined in blue indicate the outlier region from Figure 7(a). The panels demonstrate that the step-function-like behavior near $\log n = 0.36$ ($n = 2.3$) seen in Figure 7(a) is replicated separately in each range of M_*/r_e^p independent of p. Color rises rapidly near $\log n = 0.36$ ($n = 2.3$), but there is little impact of n on color above and below this value. This shows that the trends in color with M_* and M_*/r_e in the blue cloud (Figures 5(b) and (c)) are not caused by a hidden dependence on n.

(A color version of this figure is available in the online journal.)

have cross-matched the outliers to two AGN samples selected using X-ray and optical line emission data. The AEGIS region is covered by a deep 800 ks *Chandra* X-ray mosaic (Laird et al. 2009). We find that only 11 of the outliers have X-ray luminosities above 10^{42} erg s^{-1} or 7%. We have also used an optical method for selecting AGNs based on a modified version of the classical "BPT" diagram (Baldwin et al. 1981) that plots [O III]/Hβ versus $U-B$ rather than [N II]/Hα (Yan et al. 2011). This adds only 14, bringing the total to 21 AGNs, or 14% of the outliers. Thus, it seems that the vast majority of these objects are unlikely to be AGN hosts.

Another possibility is a bright blue clump of recently formed stars at the centers of the outliers, which might skew the colors and Sérsic indices as an AGN would. We would like to remind the reader that the single Sérsic GIM2D model does not fit for any substructure, such as clumps. Hence, asymmetric structures may affect the n measurements. To explore this, we constructed V and I color images of all outliers using the *HST*/ACS data and inspected them; a montage of 20 galaxies is shown in Figure 9, where each row represents a different range of $U-B$ color according to the color coding in Figure 7(a). The bluest outliers are in the bottom row. These tend to be lumpy, asymmetric, and/or small—their fitted Sérsic values are somewhat questionable. Moving up one row to the cyan points, we find a mix of genuinely concentrated galaxies plus more small galaxies like the ones in the previous row. The third row contains larger objects of intermediate color but with convincingly high concentrations. Finally, we show a sample of red sequence galaxies in the top row as a comparison; they are all red and highly concentrated spheroids.

To summarize, the blue, high-n outliers are a mix of different types. Some may have doubtful Sérsic indices, being small or with off-centered clumps of star formation or AGNs, but a fair fraction seem to be genuinely blue yet high-n galaxies. These genuine exceptions tend to be located at intermediate values of $U-B$. The existence of such outliers has been noticed before. An important class of candidates is *poststarburst galaxies* (e.g., Dressler & Gunn 1983; Couch & Sharples 1987; Poggianti et al. 1999; Goto et al. 2003). These objects possess blue colors and strong Balmer absorption yet weak Hα, signifying recent quenching, and their Sérsic indices are high (Quintero et al. 2004; Yang et al. 2008). A second class of objects is the *blue spheroidal galaxies*; like poststarbursts, they have smooth, centrally concentrated, elliptical-like profiles, but they are different in having active star formation (Menanteau et al. 2001; Im et al. 2001; Koo et al. 2005; Schawinski et al. 2009; Kannappan et al. 2009). Their masses tend to be small (Im et al. 2001), and there appear to be several objects in our outlier population that fit this description in the bottom row of Figure 9.

A quick calculation of the percentage of outliers within a volume-limited SDSS sample at $z \sim 0$ shows that it has dropped from ≈40% for our sample at $z \sim 0.65$ to ≈10% at $z \sim 0$. This difference seems consistent with the higher levels of gas at higher redshifts, which could give rise to more clumpy star formation asymmetrically distributed throughout the galaxy, skewing the Sérsic values.

For completeness, in passing we also mention satellite processes. Processes such as ram pressure stripping (Gunn & Gott 1972) and strangulation (Larson et al. 1980) do not by themselves change n. However, other satellite mechanisms involving tidal interactions (such as "harassment"; e.g., Moore et al. 1996) may induce a morphological transformation. If satellite galaxies are first harassed, they might attain a high n while still forming stars. While we do not expect most of the DEEP2 galaxies to

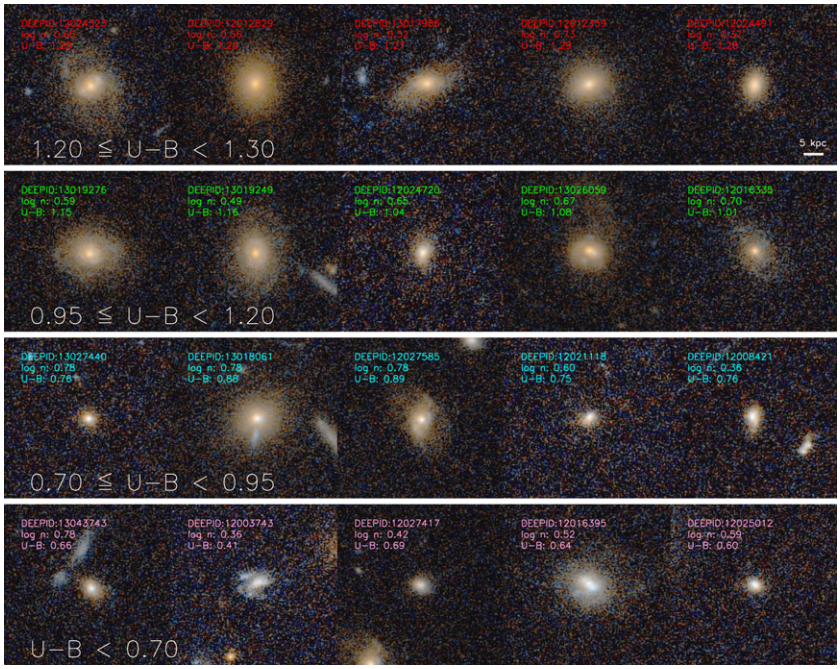

Figure 9. *HST*/ACS *V* and *I* color images for a selection of high-*n* outlier galaxies from Figure 7(a). Objects are arranged in rows according to $U-B$ color with bluer galaxies at the bottom. The bottom row corresponds to the pink points in Figure 7(a) with $U-B < 0.70$; the next row up corresponds to cyan points with $0.70 \leqslant U-B < 0.95$; and the following row is the green points with $0.95 \leqslant U-B < 1.20$. The top row contains red sequence galaxies shown for comparison; they are represented by the red points in Figure 7(a) and have $1.20 \leqslant U-B < 1.30$. A scale of 5 kpc at the average redshift ($z \approx 0.68$) of our sample is shown as a reference in the upper right picture. Many of these blue high-*n* objects seem to have Sérsic indices perturbed by small size, irregular structure, central starbursts, and/or AGNs and are cured as outliers if inner stellar surface density $\Sigma^*_{1\,\mathrm{kpc}}$ is used instead of *n*, as shown in Figure 7(b).

(A color version of this figure is available in the online journal.)

be satellites (see introduction), a more thorough investigation is needed to confirm this.

4.3.3. Inner Surface Density: An Improvement on n?

From the above, it is clear that in *n* we have found a remarkable, but still imperfect, structural predictor of quenching. The main criticism of *n* is the presence of outliers; if they could be removed, the correlation, and hence the prediction, would be nearly exact.

There are two obvious weaknesses with *n*. First, it is based on light, not stellar mass, and hence is subject to the vagaries of star formation history and dust. Second, it relies on a fit to the entire light profile and is thus at least partially dependent on the outer light distribution, which may be disturbed or irregular. In contrast, trends discovered using bulge properties in Figure 6 hint that the structure of the *inner regions* of galaxies is more important at predicting quiescence.

Accordingly, we introduce a new parameter that attempts to remove both of these weaknesses, namely, the *stellar mass surface density within 1 kpc*. This is defined as $\Sigma^*_{1\,\mathrm{kpc}} \equiv M^*_{1\,\mathrm{kpc}}/\pi r^2_{1\,\mathrm{kpc}}$, where $r_{1\,\mathrm{kpc}} \sim 1$ kpc.[30] The actual diameter used is 12 pixels (0.″36), which is set by the smallest radius that our *HST* images can conveniently resolve; it spans a radius of 1.08–1.35 kpc at our redshifts. The quantities *I* and $V-I$ are measured within this aperture, and L_B, M_*/L_B, and M_* are estimated using Equations (3), (4), and (6).

The quantity $\Sigma^*_{1\,\mathrm{kpc}}$ was already included for completeness in Figure 5 (panel (f)), where its performance is seen to be mixed. It seems to predict color less well than the global quantities M_* and M_*/r_e in the blue cloud, but it does much better than *n* in removing outliers. This is even better illustrated in Figures 7(a) and (b), which compare outliers directly. Using $\Sigma^*_{1\,\mathrm{kpc}}$, almost all the pink and cyan points have receded back into the blue cloud, and only a few green outliers remain. This suggests that the outliers in *n* are largely artifacts caused by poor GIM2D fits[31] and that using a more secure quantity like inner mass surface density can remove them. It is still true that using $\Sigma^*_{1\,\mathrm{kpc}}$ by itself is not perfect and that *n* somewhat outperforms it on the overlap criteria seen in Figures 5(e) and (f). That a genuine spread exists in $\Sigma^*_{1\,\mathrm{kpc}}$ is confirmed by ongoing work with higher-S/N SDSS data (J. J. Fang et al. 2012, in preparation), which, however, reveals some additional striking regularities. Our point for now is that using $\Sigma^*_{1\,\mathrm{kpc}}$ removes the large number of outliers that are present with *n*. Furthermore, the definition of $\Sigma^*_{1\,\mathrm{kpc}}$ as an *inner* mass density directs our attention even more strongly to the fact that it is conditions *near the center of the galaxy* that drive quenching.

5. DISCUSSION

In this paper, we have found that the most discriminating parameter of quiescence, according to the measures of the overlap region, is the Sérsic index, and that a plot of color versus Sérsic index shows a step-like behavior near $n = 2.3$, suggestive of some sort of genuine quiescence threshold. About 40% of the $n > 2.3$ galaxies, however, are "outliers" that fall outside this behavior. These outliers have central mass densities much lower than those of the red sequence and fully consistent with those of the blue cloud. In other words, under this new

[30] Note that here we include the π, so these are physical surface densities.

[31] GIM2D only models a galaxy into either a bulge+disk model or a single Sérsic model. More complex structures like spiral arms, bars, and clumps are not modeled. Thus, a galaxy with these features is potentially ill fit.

parameter, $\Sigma^*_{1\,\mathrm{kpc}}$, the outliers now fall in line, suggesting that a galaxy's central structure may be even more physically related to quiescence than Sérsic index.

Both n and $\Sigma^*_{1\,\mathrm{kpc}}$ corroborate our second major finding that most blue cloud galaxies at the observed epoch cannot simply fade onto the red sequence. We have shown through stellar mass measurements of bulges and disks that the red sequence galaxies have absolutely higher bulge *mass* concentrations, i.e., that the jump in n is not due simply to the fading of disks (see Section 4.2). The central mass densities extend this conclusion to the very centers of galaxies. In other words, the transition to the red sequence involves a significant restructuring of a blue cloud galaxy's *innermost stellar density profile*.

Below the critical value of $n = 2.3$, however, Sérsic index shows little to no correlation with star formation, and color is more closely correlated with M_*/r_e (or perhaps with M_*; see Figure 5).

This two-pronged behavior suggests that the star formation history of a galaxy is shaped by two separate factors at different stages. While the object is still star forming (in the blue cloud), its star formation rate depends on *global* parameters, like M_*/r_e or M_*. Then, a major internal mass reorganization occurs, a dominant bulge forms, and star formation stops. In the following discussion, we compare these results to the predictions of the standard merger model for bulge building and quenching and find reasonable agreement, but also several issues. To alleviate these issues, we also consider other models, specifically, violent disk instability (Noguchi 1999; Elmegreen et al. 2008; Dekel et al. 2009), secular evolution (Kormendy & Kennicutt 2004), morphological quenching (Martig et al. 2009), and halo quenching (Silk 1977; Rees & Ostriker 1977; Blumenthal et al. 1984; Birnboim & Dekel 2003; Kereš et al. 2005; Dekel & Birnboim 2006; Cattaneo et al. 2006). We end with a brief discussion on an unresolved concern.

5.1. Merger Model

Major mergers[32] have been linked to the formation of spheroids since Toomre & Toomre (1972), with considerable work in the years since (see Hopkins et al. 2009b and references therein). The process of bulge formation in classical merger models occurs through both the violent relaxation of pre-existing stars to the center and a gaseous dissipation-induced nuclear starburst (Hopkins et al. 2009b).

Comparison of the bulge-dominated products of these simulations to observed early-type galaxies shows good agreement. The Sérsic indices of the merger products from Hopkins et al. (2008) are high, $n \gtrsim 2.5$. Similarly, Naab & Trujillo (2006) showed that their disk mergers (with bulges) created galaxies with $3 < n < 4$.[33] Both of these works produce spheroids with Sérsic indices in the range of our red sequence spheroids and of other observations (e.g., Kormendy & Kennicutt 2004; Drory & Fisher 2007; Fisher & Drory 2008).

The properties of quenching induced by mergers are also consistent with our data. The merger model predicts that quenching occurs through the nuclear starburst (Mihos & Hernquist 1994), in which a large portion of the gas[34] is exhausted (depending on gas fraction; see Springel & Hernquist 2005; Okamoto et al. 2005; Robertson et al. 2006; Cox et al. 2008; Governato et al. 2007, 2009), and through subsequent feedback, from supernovae and/or AGNs (Springel et al. 2005; Murray et al. 2005; Ciotti et al. 2009). Note that both sources of quenching originate *from the center of the galaxy*, suggesting that the conditions at the center may correlate better with the quenching state than global properties. This is what we find. Furthermore, the central surface mass densities of the simulated spheroids from Hopkins et al. (2009a) match our observations of the red sequence spheroids in Figure 7(b)—with values of $\log \Sigma = 9$–$10\ M_\odot\ \mathrm{kpc}^{-2}$ at 1 kpc.

A further success of the merger hypothesis is the good match between it and the stellar mass range where bulge building is observed to occur. A major point is that the efficiency of bulge building from major mergers is expected to be highly dependent on the *pre-merger gas fraction*, such that decreasing gas content increases the potential to form bulges (Springel & Hernquist 2005; Robertson et al. 2006; Hopkins et al. 2009b). This dependence is consistent with the assumption that gas content gradually falls as galaxies age in the blue cloud, making them ultimately ripe for spheroid formation via mergers. Because more massive galaxies exhaust their gas quicker due to the phenomenon known as "downsizing" (e.g., Cowie et al. 1996), there is a strong color–mass relation in the blue cloud, meaning that the reddest blue cloud galaxies at any epoch have the least amount of gas. According to the merger model, this means that they are also on the threshold of forming bulges.

Evidence for this hypothesis is strong in Figure 5(b), which shows a remarkably tight correlation between stellar mass and color in the blue cloud in the sense that more massive galaxies are the reddest. Further data come from Catinella et al. (2010) and Saintonge et al. (2011), who presented HI and CO data in the GASS and COLD GASS survey, respectively. These works illustrate that the average atomic and molecular gas fractions of galaxies do decrease with increasing stellar mass and increasing $NUV - r$ color. Although these surveys do not fully sample the blue cloud (these surveys only observe $M_* > 10^{10}\ M_\odot$ galaxies), extrapolating these seemingly linear trends to lower masses indicates that total gas fraction does indeed decrease with mass along the blue cloud. Theoretically, Hopkins et al. (2010a) showed that the most effective bulge-building major mergers are clustered around $\log M_* \sim 10.5\ M_\odot$ at $z \sim 1$, which is in the center of the overlap region of M_*. This behavior is due in part to exactly the same reason, namely, decreasing gas content as galaxies age within the blue cloud. In a general way, then, theory predicts that galaxy colors and gas contents should both age within the blue cloud, causing galaxies to become more prone to bulge-building mergers at higher mass and low gas level, and these trends broadly agree with the observations.

In detail, however, the data indicate that M_*/r_e is a better predictor of quenching than M_* alone (cf. overlap regions in Figure 5(b) versus Figure 5(c)). This may be because M_*/r_e is related to velocity dispersion (Franx et al. 2008; see footnote 26), which, based on a new study by Wake et al. (2012a), is the galaxy property most closely related to halo mass. This finding could then be a manifestation of the dependence of quenching on a critical halo mass. Alternatively, it may reflect the fact that

[32] According to Hopkins et al. (2010a), major mergers dominate the formation and assembly of $\sim L_*$ bulges and the total spheroid mass density. Thus, we only consider major mergers in this discussion. However, it should be noted that minor mergers can create bulges (Bournaud et al. 2007) and do contribute a non-negligible amount (~30%) to the total spheroid mass density (Hopkins et al. 2010a).

[33] Naab & Trujillo (2006) conducted a collisionless simulation that does not include gas and thus does not model a nuclear starburst component. That is why their pure disk–disk mergers only have $n \approx 1.5$, because they lack the high central surface brightness typical of dissipative gas-rich mergers.

[34] In the following discussion, gas is assumed to be cold gas unless otherwise stated.

radii are shrinking as stellar mass builds up in the centers of quenching galaxies and thus reflects a property of the galaxies themselves rather than of their halos. We elaborate further on these thoughts in Section 5.5.

Although there are some aspects of the merger model that match our data, general agreement on the validity of this model has not been reached. One controversial issue is whether major mergers can actually quench galaxies. There have been various works that support this idea (e.g., Schawinski et al. 2007; Alexander et al. 2010; Cano-Diaz et al. 2012; Farrah et al. 2012). In particular, Cano-Diaz et al. (2012) obtained VLT-SINFONI integral-field spectroscopy for one quasar at $z = 2.4$ and showed a suppression of narrow Hα emission, a tracer of star formation, in the region with the highest outflow velocity and highest velocity dispersion. But this is only one example and does not erase the contradicting evidence others have offered. For example, using a sample of X-ray and post-starburst galaxies from SDSS and DEEP2 at $0.2 < z < 0.8$, Coil et al. (2011) found winds with velocities that are insufficient to shut down star formation, indicating that the presence of an AGN does not produce faster winds, nor does it seem to play a major role in quiescence. And Ammons et al. (2011) fail to find any correlation between host galaxy color and X-ray hardness ratio among $z = 0.5$–1.5 galaxies, as might be expected from the blowout model.

Another important concern is whether there are enough mergers to account for the bulge density in the universe. Studies that have measured the galaxy merger rate often present different results (e.g., Bell et al. 2006; Conselice 2006; Lin et al. 2008; Lotz et al. 2008b; Bundy et al. 2009; Xu et al. 2012; Bluck et al. 2012). Lotz et al. (2011) addressed the issue of disparate observational merger rates; they found that the major reason for these differences is the assumed timescale in which a merger is observable. Using a suite of hydrodynamic merger simulations, they constrained the observable timescales of three common merger rate estimators—close galaxy pairs, G/M_{20}, and asymmetry—and found that if a physically motivated average observability timescale was adopted to calculate the merger rates, then these rates become largely consistent. The remaining differences between the merger rates are explained by the differences in the ranges of mass ratio measured by different techniques and the differing parent galaxy selection.

Additionally, for mass-limited samples ($M_* > 10^{10}\ M_\odot$), they found excellent agreement between their merger rates from close pairs and several theoretical merger rates. Specifically, they agreed with the merger rates of Hopkins et al. (2010a), who, using a combination of semi-empirical models and high-resolution merger simulations, concluded that there are enough major mergers, to within a factor of $\sim$2, to account for the observed growth of the bulge population. They argue that previous studies reached different conclusions because they assumed incorrect merger timescales; rather, if a uniform simulated-calibrated merger timescale is used, then many of these works actually come to their conclusion (see also Robaina et al. 2010).

An alternative way to address whether there are enough mergers is to examine the phase in galaxy evolution that is predicted to correspond to the period of mergers. Adopting a simplified model in which blue star-forming galaxies merge and transform into red quiescent galaxies, one would expect a short period in which galaxies have intermediate colors, i.e., they are in the green valley. A recent study on the morphologies of green valley galaxies by Mendez et al. (2011) found that only 14% of the galaxies in their sample are identified as ongoing major or minor mergers (using G/M_{20} and asymmetry parameters), which is lower than the 19% merger rate in the blue cloud. They further found that most green valley galaxies have disks and that 21% have $B/T < 0.05$, implying that they were unlikely to have experienced a recent major merger.

To conclude, while the merger model fits many aspects of our data, there are serious open questions, including whether major mergers are able to quench, whether there are enough of them, and whether they are consistent with the color and morphologies of green valley galaxies. In the remaining discussion, we explore other models that may alleviate these problems.

5.2. Disk Instabilities: Violent and Otherwise

An alternative bulge-building process involves the growth of giant clumps formed via gravitational instability in gas-rich disks (Noguchi 1999; Elmegreen et al. 2008; Dekel et al. 2009; Ceverino et al. 2010). These clumps migrate inward and coalesce to form a bulge, and simulations suggest that galaxies can develop classical bulges with $n \approx 4$ during this process[35] (Elmegreen et al. 2008). Recent simulations also show that these clump-origin bulges have central surface mass densities comparable to that of our red sequence galaxies (D. Ceverino et al. 2012, in preparation). The effectiveness of this instability, however, is highly dependent on the gas inflow rate onto the galaxy (Dekel et al. 2009), which declines with time. Thus, we expect this process to be more important at redshifts higher ($z \sim 2$) than that of our sample.

Although this process may have operated strongly at $z \sim 2$, we stress that this paper concerns a different sample of galaxies at lower redshift when conditions may have changed. Bell et al. (2004b) and Faber et al. (2007) found that the number of red sequence galaxies has at *least* doubled from $z \sim 1$ to $z \sim 0$, indicating that a fraction of our galaxies at $z \sim 0.65$ are actively migrating to the red sequence as we view them. Using the NEWFIRM survey, Brammer et al. (2011) found that the mass density of quiescent galaxies with $M_* \gtrsim 3 \times 10^{10}\ M_\odot$ increased by a factor of $\sim$10 from $z \sim 2$ to the present day. Similarly, Hopkins et al. (2010b) argue that the vast majority of ellipticals/spheroids do *not* form through high-redshift channels. They state that the observed mass density of bulge-dominated galaxies at $z \sim 2$ is only $\sim$5% of its $z = 0$ value, and at $z \sim 1$, it is still only $\sim$20%–35% of its $z = 0$ value. Thus, most bulges are formed at $z \lesssim 1$, meaning that the majority of our red sequence galaxies are recent arrivals.

Although we expect violent disk instabilities to be increasingly less frequent at decreasing redshift, owing to lower gas fraction, the actual bulge contribution due to this mechanism at $z < 1$ is currently unknown. Hints at intermediate redshift suggest that the process may not be limited to high z. For example, Bournaud et al. (2012) found that *half* of a sample of $z \sim 0.7$ disk galaxies are clumpy without any merger signatures, implying that disk instabilities could still be important at that redshift.

Perhaps we need to think more broadly and to recognize that the settling of matter to form regular, axisymmetric disks is a very lengthy process lasting many billions of years. When any non-axisymmetric forces exist, an inevitable outcome is that *some* mass will be driven to the center. Furthermore, in a general way the higher the degree of non-axisymmetry in the

[35] However, a recent paper by Inoue & Saitoh (2012) claims that these clump-origin bulges are more akin to pseudobulges in that they exhibit $n < 2$.

potential, the higher the rate of matter inflow will be. At late times, non-axisymmetry has become small and the flow rate is low, a process that we call "secular evolution," which we discuss next.

Future studies will resolve this question.

5.3. Secular Evolution

Secular evolution (Kormendy & Kennicutt 2004) constitutes the weak end of the spectrum of non-axisymmetric processes in disk evolution. This complex of processes involves the slow rearrangement of gas (and stellar) mass due to gravitational interactions between the gas and stars within a disk galaxy. A variety of relatively weak non-axisymmetric disturbances, such as bars, ovals, and spiral structure in the stellar component, can create non-central gravitational forces that add or subtract angular momentum from the gas, which responds by moving inward or outward depending on radius. The process sweeps inner gas into the center, where it forms stars, and pushes gas farther out to larger radii, where it can accumulate in tightly wrapped spiral arms or a ring (Simkin et al. 1980; Kormendy & Kennicutt 2004). Separately, the gas itself may become mildly gravitationally unstable, which raises the velocity dispersion and causes the gas to radiate. This net loss of energy must come from somewhere, and the gas responds by sinking slowly to the center, increasing its (negative) potential energy (Forbes et al. 2012). Overall, these processes push some mass to the center and other mass to the outskirts, thus increasing n. The forces are, however, weak and the process is slow, hence the term "secular evolution." The total time required would be many dynamical timescales and thus at least several Gyr (Kormendy & Kennicutt 2004; Fisher et al. 2009).

Although secular evolution may contribute to some of the bulge building taking place at $z \sim 0.65$, we do not believe it is the major factor. According to Kormendy & Kennicutt (2004), bars are a major driver of secular evolution at the current epoch. Assuming that bars are also the main drivers at higher redshifts, comparing the bar fraction from the past, which is 10%–25% among late-types at $z > 0.8$ (Jogee et al. 2004; Sheth et al. 2008; J. Herrington et al. 2012, in preparation), to the current epoch, which is 30%–60% at $z \sim 0$ (Sheth et al. 2008; Cameron et al. 2010; Masters et al. 2011), implies that secular evolution was not a major bulge-building process at $z \sim 0.65$. Additionally, Koo et al. (2005) showed that 85% of luminous field bulges within this redshift range are red, arguing against secular evolution being the dominant bulge-building process since they are expected to mainly produce blue bulges (Kormendy & Kennicutt 2004).

Finally, the physical structure of bulges built by secular evolution differs strongly from ones built by mergers, as reviewed by Kormendy & Kennicutt (2004). The so-called classical bulges built by mergers resemble small ellipticals embedded in disk galaxies. They have high stellar velocity dispersion and high vertical extent above the plane, having been "fluffed up" by the merger—in other words, they are true spheroids. They can also be very massive and contain a considerable fraction of the total mass of the galaxy. In contrast, the "bulges" built by secular evolution are relatively flat, have effective radii of only a few hundred pc, and have low fractional masses. Because of these differences, Kormendy & Kennicutt (2004) term these structures "pseudobulges." Drory & Fisher (2007) directly compare the properties of these two types of bulges. They isolated a sample of nearby, massive, disk galaxies and classified them into classical bulges and pseudobulges based on the morphology of the central regions. Confirming their disparate nature, they found a clear bimodality in that pseudobulge galaxies are much bluer (in the blue cloud or green valley), have low central surface brightness, and have low global Sérsic index ($n < 2.5$).

For these reasons, we conclude that the pseudobulges cannot be an important contributor to our intermediate-redshift, high-n, red sequence galaxies. They may, however, certainly help build the bulges seen in late-type galaxies, becoming increasingly more important with decreasing redshifts, where the bar fraction can be as high as 60% (Sheth et al. 2008).[36] In fact, Fisher & Drory (2011) show that, by number, 80% of the bulges within 11 Mpc of the Milky Way are actually pseudobulges. But, by mass, they only make up $\lesssim$10% of the total mass density in local spheroids (Allen et al. 2006; Driver et al. 2007).

In conclusion, we find it helpful to think of the entire family of bulge-building mechanisms as ordered along a "disturbance continuum" from severe to mild, with corresponding timescales from short to long and bulge-building rates from fast to slow. The members of this continuum consist of major to minor mergers at the strong end, through violent disk instabilities, to milder disk instabilities, and finally to weak, secular instabilities like bars, spiral arms, and normal star formation. The dividing line between an externally triggered process like mergers and internally triggered dynamical instabilities is fairly clear, but there is no such dividing line among the internal processes—each one shades smoothly into the next. However, since every disk is sooner or later subject to one or more of these processes, the central densities of disks *inevitably* tend to increase—the only question is, how fast?

We note that this disturbance continuum is also a continuum in time, with early galaxies experiencing disturbances at the strong end of the spectrum and later galaxies settling down to slower, more secular rates. Our AEGIS galaxies exist somewhere near the middle of the time continuum, when disky galaxies as a class were considerably more disorganized and more non-axisymmetric than they are today. This logic further supports our conclusion above that secular processes were probably not the major bulge-building process in these galaxies, with a combination of mergers and stronger disk instabilities being more likely. However, the exact balance of these two processes remains for further study.

5.4. Morphological Quenching

The preceding sections focused on mechanisms to increase the central densities of disk galaxies and thus account for one of our major findings, namely, higher central stellar densities in quenched galaxies. Even though a variety of stellar buildup mechanisms were identified, including mergers and internal instabilities, we tacitly assumed regardless of process that high density would always lead to the creation of a black hole and that feedback from the black hole would quench star formation. However, the discussion in Section 5.1 noted a lack of conclusive evidence that AGN feedback actually quenches star formation in disk galaxies. In this section and the next, we review two other quenching mechanisms that have been proposed to operate in central galaxies.

The first of these is morphological quenching (Martig et al. 2009), whereby the steep potential well of a bulge is able to drive

[36] This number is controversial; recent studies by Nair & Abraham (2010), Masters et al. (2011), and Lee et al. (2012) show that the local bar fraction is ∼30%.

the Toomre Q parameter above unity and stabilize the gas disk against star formation. An attractive aspect of morphological quenching is that it sets in when n is high, which jibes with the structure of quenched galaxies. This mechanism is unique because it does not require the removal of gas or the suppression of the cold-gas supply onto the galaxy. Instead, gas can continue to accrete onto a galaxy yet remain inert to star formation owing to the strong central mass concentration. A recent analysis of a set of three high-resolution AMR simulations at $z \simeq 2.3$ by Ceverino et al. (2010) demonstrates this process. From $z \simeq 2.3$ to $z \sim 1$, two of these galaxies are shown to evolve from a gravitationally unstable and turbulent disk into a stable system; they attribute this change to presence of a dominant stellar bulge.

An explicit prediction of morphological quenching is that red, early-type galaxies could host significant cold gas in the amount of a few percent of their baryonic mass, and in fact comparable to gas fractions in normal star-forming galaxies (Martig et al. 2009). However, this prediction is not consistent with observed H I properties of nearby early-type galaxies. Though H I is frequently detected, especially in field galaxies (Morganti et al. 2006; Oosterloo et al. 2010), the amounts are nearly always low. This is confirmed by the GASS H I survey at Arecibo of ∼1000 slightly more distant massive galaxies with $M_* > 10^{10}\ M_\odot$ (Catinella et al. 2010), which shows that the average H I fractions of red sequence galaxies are at least 10 times lower than galaxies of similar mass on the star-forming main sequence (Schiminovich et al. 2010; Fabello et al. 2011). The same result applies to molecular H_2 in the same galaxies (Saintonge et al. 2011). These recent studies simply confirm what has been known for a long time about early-type galaxies—that their absolute gas contents are low compared to star-forming galaxies (e.g., van Driel & van Woerden 1991; Roberts & Haynes 1994; Noordermeer et al. 2005). Hence, in order to achieve quenching, it is necessary to reduce the fractional gas content, by either expelling gas or preventing new gas from falling in—morphological quenching alone cannot do the job.

For the nearest galaxies it is possible to map the H I distributions (van Driel & van Woerden 1991; Noordermeer et al. 2005; Morganti et al. 2006; Oosterloo et al. 2010). Normal lenticular galaxies typically have H I in an outer ring with an empty hole in the middle. Several authors (van Driel & van Woerden 1991; Cortese & Hughes 2009; Oosterloo et al. 2010) have stressed that the surface density of gas in these rings is well below the critical threshold for star formation (Kennicutt 1989; Schaye 2004; Bigiel et al. 2008), which represents the threshold for molecular H_2 formation, a tracer of gravitationally unstable gas (e.g., Krumholz et al. 2011). Moreover, the predicted star formation efficiency at such low densities is 10 times lower than in normal star-forming galaxies (Krumholz et al. 2012), which agrees well with the low star formation efficiencies seen in the Arecibo GASS survey (Schiminovich et al. 2010; Fabello et al. 2011). Such low-level star formation has recently been detected in the outer disks of normal green-valley S0 galaxies in *HST* U imaging (Salim & Rich 2010; Salim et al. 2012; J. J. Fang et al. 2012, in preparation).

Hence, we reach a very important conclusion about the evolutionary track of quenching: low gas content is the underlying cause of quenching, but star formation shuts down even faster as gas content falls below the threshold value, owing to the nonlinear relation between cold gas surface density and star formation rate. This fall in star formation efficiency causes galaxies to redden even faster than expected, propelling them rapidly to the red sequence.[37]

It is fair to point out that all of the data cited above to evaluate morphological quenching come from nearby galaxies, some of which are members of virialized clusters and dense groups that are subject to environmental processes such as ram-pressure stripping or strangulation. However, many of the nearest galaxies are known *not* to be in clusters (e.g., Oosterloo et al. 2010), and there must also be many field objects among the thousand or so galaxies in GASS, yet the trends are the same. In short, we cannot think of any reason why morphological quenching would be the key causative agent for quenching at higher redshift when it does not appear to play that role (even for field galaxies) today.

5.5. Critical Halo Mass

The termination of the cold gas supply due to a critical halo mass is commonly referred to as "halo quenching" (Silk 1977; Rees & Ostriker 1977; Blumenthal et al. 1984; Birnboim & Dekel 2003; Kereš et al. 2005; Dekel & Birnboim 2006; Cattaneo et al. 2006). Halos below $\sim 10^{12}\ M_\odot$ are able to accrete gas through cold flows, while halos above the threshold mass experience a virial shock that heats the gas. The hot, diluted gas in massive halos is vulnerable to feedback from AGNs, which effectively halts star formation. An interesting outcome of this theory is the ability to generate a hot halo atmosphere that allows for AGN "radio mode" feedback (Croton et al. 2006; Dekel & Birnboim 2006). This mechanism provides a way to permanently quench a galaxy, which is desirable since the stellar populations of most local ellipticals show no signs of recent star formation (since at least $z \sim 1$; Thomas et al. 2005), despite continual gas infusion by stars.

Various studies have explored this theory. For example, using a data-driven, halo-abundance matching technique that spans $0 < z < 1$, Conroy & Wechsler (2009) found a gradual transition of galaxy properties—including SSFR—across a halo mass of $\sim 10^{12}\ M_\odot$. Recently, More et al. (2011) inferred the halo-mass–stellar-mass relation based on kinematics of SDSS satellite galaxies and found that red, central galaxies, on average, occupy more massive halos than blue centrals for fixed luminosity but show a less appreciable difference for fixed stellar mass. Woo et al. (2012) study the quenched fraction of central galaxies as a function of halo mass and find that the span of halo masses between 20% quenched fraction and 60% quenched fraction is a whole 1.5 dex. This agrees well with the width of 0.8 dex seen here in the overlap region using stellar mass (and the same quenched fractions) in Figure 5(b) and the theoretical scaling law between central and halo mass (Kang et al. 2005; Cattaneo et al. 2006). By contrast, the width using our preferred parameter, inner surface density, is only 0.5 dex (cf. Figure 5(f)). An interpretation that emerges from these works is that halo mass has a gradual and probabilistic effect on galaxy properties, which is therefore very consistent with a wide overlap region in halo mass. Instead of a sharp transition at $\sim 10^{12}\ M_\odot$, galaxies seem to become ready for star formation quenching around this critical value, followed by some type of event that ultimately triggers quenching.

[37] An interesting corollary comes from the fact that UV colors are more sensitive to weak star formation than optical colors, and thus galaxies can be on the red sequence according to $U-B$ but in the green valley according to $NUV-r$; this is actually seen (e.g., Salim & Rich 2010; Salim et al. 2012). Since galaxies in this paper are classified using $U-B$, it is possible that some of our red sequence objects would appear in the green valley if near-UV color were used.

This scenario ties in well with our two-stage picture in which galaxies "ripen" along the blue cloud, becoming more and more susceptible to quenching as they age. In Section 5.1, we associated this ripening with decreasing gas content with stellar mass in the blue cloud, which is also seen in our data as an increase in $U-B$ with stellar mass (Figure 5(b)). Lower gas content means that less gas needs to be removed in quenching, which means in turn that more massive blue cloud galaxies are more vulnerable to quenching. Their lower gas content stems from the fact that their halo masses are closer to the critical value $\sim 10^{12}\ M_{\odot}$, the neighborhood where cold accretion shuts down. This basic picture does not change if M_*/r_e (Franx et al. 2008) or central velocity dispersion (Wake et al. 2012a) is substituted for stellar mass—any parameter that tracks halo mass reasonably well can serve as a ripeness indicator.

This logic leads to a picture in which the changes in gas fraction, color, and star formation rate along the blue cloud are caused by the gradual dominance of shock-heated gas over cold streams as galaxies near the critical halo mass. A tougher challenge, though, is to explain why the actual quenching state relates so closely to conditions *at the center of the galaxy*—why is this link so close if the primary governor of cooling is out in the halo?

We have no firm answer to this but offer some speculations. Evidently the central conditions either signal or even trigger a second quenching mechanism, and this, plus "natural" halo quenching, is what tips a galaxy over the edge. The obvious candidate for this second process is AGN feedback, but we have stressed that direct evidence for this is still weak. It is good to be cautious since the ERIS Milky Way simulation (Guedes et al. 2011) develops a red bulge and high central stellar density quite naturally through mergers and/or internal disk evolution. Its star formation rate is falling, and it seems well on its way to the red sequence, all without benefit of AGN feedback.

Ideal would be some mechanism that both correlates with central density and can switch a halo quickly from cold mode to hot mode. Some possibilities come to mind. Perhaps AGN feedback helps to heat the halo. Perhaps exhaustion of gas at the center enhances the ability of stellar winds to sweep gas out of the galaxy. Finally, perhaps a merger simultaneously builds up central stellar density *and* triggers a full standing shock. Such a transformation is seen in simulations (A. Dekel et al. 2012, in preparation) where a minor merger triggers a shock that expands from the halo center to the virial radius and heats the medium. The larger point is that quenching is probably not just one factor but a combination of factors that build to some critical threshold.

5.6. The Relationship Between Color and Star Formation

In this section, we broach the lingering issue of the relationship between color and star formation. Throughout this paper, we have constantly interchanged these two parameters, suggesting that color is a good representation of SSFR. However, the issue of dust has not been thoroughly addressed in our colors. Although we have excluded edge-on galaxies (which are presumably highly affected by dust) and ensured that our red sequence galaxies are truly quiescent (using the *UVJ* diagram; see Section 3), we have not actually made any dust correction to our rest-frame $U-B$ colors. Therefore, the color trends that we have examined throughout this paper may not exactly translate into star formation trends. The analysis most affected would be our interpretation of how the star formation rates of galaxies behave within the blue cloud. We remarked on the tight trend between color and M_*/r_e (and M_*) within the blue cloud in Figure 5(b) (and Figure 5(c)), and we proposed that star formation must decrease with M_*/r_e (or M_*). However, this color trend may instead be due to more dust in larger galaxies. If this is the case, then a galaxy's star formation would be independent of M_*/r_e (or M_*) within the blue cloud. However, work using dust-corrected or dust-robust multi-wavelength data (e.g., Noeske et al. 2007; Salim et al. 2007; Schiminovich et al. 2007; Zheng et al. 2007) has shown that SSFR does indeed decrease with increasing stellar mass, which is what we have inferred from our color–mass diagram (Figure 5(b)). Thus, these works justify our subtle assertion that color is a proxy for star formation. Most importantly, though, our lack of dust-corrected $U-B$ colors does not affect our main result that the inner stellar structure of galaxies is most related to quiescence, since our quenching analysis is based on differentiating galaxies on the blue cloud from those on the red sequence, which we have ensured to be unaffected by dust (see Section 3).

6. CONCLUSION

In this paper, we analyze a sample of DEEP2/AEGIS galaxies in the redshift range $0.5 \leqslant z < 0.8$ using *HST*/ACS V, I images. Our sample has been run through GIM2D, a bulge+disk decomposition program that gives us information on the subcomponents of intermediate-redshift galaxies. Using these data, which we provide at http://people.ucsc.edu/~echeung1/data.html, our goal is to address how quenching depends on galactic structure.

Our methodology is to assess the color correlations of several structural parameters—M_*, M_*/r_e, M_*/r_e^2, n, and $\Sigma^*_{1\,\mathrm{kpc}}$—by computing an "overlap region," which is the band in color-parameter space that encompasses both red and blue galaxies. To quantify overlap regions, we calculate the fractional number of galaxies within the overlap region $\Delta N/N$ and the fractional extent of the region $\Delta x/x$; the parameter with the smallest overlap region is considered to be the best predictor of quiescence. Finding that no parameter is a perfect predictor of quenching, we explore the overlap region of M_*/r_e for secondary color correlations among a variety of other parameters, including those of bulge and disk. We also consider the number of severe outliers from the best predictor of quiescence, n. Our results are the following:

1. The Sérsic index (n) most sharply discriminates between the red sequence and the blue cloud. Eliminating dusty, red sequence contaminants ensures that n targets quiescent galaxies, not merely red ones. Moreover, the color-n diagram resembles a step function, suggesting that n is related to a physical quenching threshold.
2. However, there are exceptions to this general behavior—blue galaxies make up ≈40% of our $n > 2.3$ galaxies. Suspecting contamination from starbursts, AGNs, and/or other sources of error, we measured central surface stellar mass densities, which revealed that these outliers do not truly belong with the red sequence—their $\Sigma^*_{1\,\mathrm{kpc}}$ are much lower. Central surface density corrects these outliers and hints that it is the *inner* structure of galaxies that is most related to quiescence.
3. Red sequence bulges are roughly twice as massive as blue cloud bulges at the same galaxy stellar mass (and M_*/r_e), yet also roughly twice as small. This structural difference shows that most blue galaxies at the observed epoch do not simply fade onto the red sequence. Rather, the high values of n and $\Sigma^*_{1\,\mathrm{kpc}}$ on the red sequence must reflect a net

migration of existing stars toward the center of the system or the formation of new stars at the center. This restructuring either causes quenching itself or is closely related to the process that does.

4. While in the blue cloud before quenching, a galaxy's star formation rate is most closely correlated with M_*/r_e (or with M_*).

These results suggest that galaxies evolve toward the red sequence in a two-stage process. In stage one, a galaxy is star forming in the blue cloud at a rate that correlates with global parameters like M_*/r_e (or M_*). Since these in turn reflect halo mass, a broad conclusion might be that star formation is controlled by the galaxy's halo while stars are still forming. As stellar mass increases, the halo mass also increases, ultimately approaching the critical value $\sim 10^{12}\ M_\odot$, where cold flows begin to give way to hot gas, which cannot accrete. The gas content of the galaxy begins to fall as it nears this critical value, and colors redden.

The result of stage one is a galaxy that is increasingly vulnerable as time goes by to the onset of a second quenching process. This second process must be closely associated with bulge building, and central stellar density, $\Sigma^*_{1\,\mathrm{kpc}}$, must increase. AGN feedback is an obvious candidate for this second process, but direct evidence for this is still weak. Also unclear is the exact mechanism that leads to the central mass buildup at the center of the galaxy. We have stressed that galaxies, particularly at high redshift, are far from axially symmetric and that any non-axisymmetry leads inevitably to an exchange of angular momentum and/or loss of energy, which causes some stars and gas to move inward. Major mergers sit at the strong end of this "disturbance continuum"; secular evolution processes sit at the other end; and minor mergers, violent disk instabilities, and milder disk instabilities sit in the middle. Given that our galaxies lie at $z \sim 0.65$, where galaxies are still moderately disturbed, it is unlikely that secular evolution plays a major role in them. More likely is some combination of mergers and disk instabilities, which collectively are probably strong enough and frequent enough to do the job. Mergers in particular have several well-known advantages: they build bulges at the right stellar mass, they naturally build a concentrated stellar spheroid, they drive a lot of gas quickly to the center that can power an AGN or starburst, and they may be able to quickly switch a marginally cooling halo into hot mode. A problem for major mergers is the large fraction of galaxies in the green valley that are disky, but these might be explained by the other mechanisms, or they might be reddened members of the blue cloud.

One conclusion seems clear, and that is that moving into the green valley and thence to the red sequence requires a lowering of fractional cold gas content. This can only be achieved either by expelling gas or by preventing its infall. Exactly how this happens is still not clear, but at least some of the parameters surrounding the process are better known.

We thank Thiago Signorini Gonçalves, Stijn Wuyts, Joanna Woo, Alexis Finoguenov, Jonathan Trump, and Lia Athanassoula for useful comments. We also thank the anonymous referee for a very helpful report that resulted in substantial improvements to the paper.

The DEEP2 survey was initiated under the auspices of the NSF Center for Particle Astrophysics. Major grant support was provided by National Science Foundation grants AST 95-29098, 00-711098, 05-07483, and 08-08133 to UCSC and AST 00-71048, 05-07428, and 08-07630 to UCB. The DEEP2 survey has been made possible through the dedicated efforts of the DEIMOS instrument team at UC Santa Cruz and support of the staff at Keck Observatory. The *HST* ACS mosaic in EGS was constructed by Anton Koekemoer and Jennifer Lotz and was funded by grant HST-AR-01947 from NASA. Finally, we recognize and acknowledge the highly significant cultural role and reverence that the summit of Mauna Kea has always had within the indigenous Hawaiian community; it has been a privilege to be given the opportunity to conduct observations from this mountain.

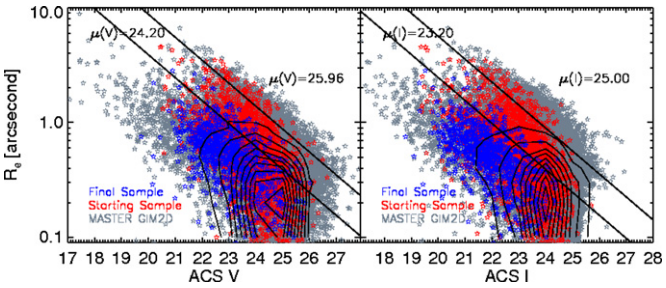

Figure 10. Semimajor axis effective radius in arcsecond is plotted against *V* and *I*. The two lines of constant surface brightness in each panel roughly mark the edge of the "starting" and "final" samples' surface brightness distribution. The contours represent the number density of the master GIM2D sample.

(A color version of this figure is available in the online journal.)

APPENDIX A

SURFACE BRIGHTNESS LIMITS

One might be concerned that our "final" sample may be missing low surface brightness galaxies; in this Appendix, we show that this is not the case. We demonstrate our "final" and "starting" samples' surface brightness limits in Figure 10 by plotting the effective radius in arcseconds versus *V* and *I* (see Section 3 for sample definitions). The master GIM2D sample is plotted in gray, and the "starting" and "final" sample are overplotted in red and blue, respectively. In each panel, we draw two lines of constant surface brightness to give an idea of our samples' surface brightness boundaries. There is obviously an edge to the distribution of the master GIM2D sample at low surface brightnesses. Whether this is a selection limit or a reflection of where real galaxies lie is unclear. But it is clear that the master GIM2D sample contains galaxies with the lowest surface brightnesses, indicating that our "starting" and "final" samples are sensitive to them.

In these plots, the relevant difference between the "starting" and "final" sample is the imposed mass limit of the "final" sample. The main concern in terms of sample completeness boils down to whether the "final" sample is missing massive low surface brightness galaxies. It is clear that there are many galaxies in the "starting" sample (and the master GIM2D sample) with much lower surface brightnesses than those in the "final" sample. Hence, if such massive low surface brightness galaxies existed, the "final" sample should certainly contain them, and thus our "final" sample does not miss low surface brightness galaxies.

APPENDIX B

GIM2D MEASUREMENT QUALITY

In this appendix, we show that the errors on the GIM2D measurements are well behaved even at the sample limits. The

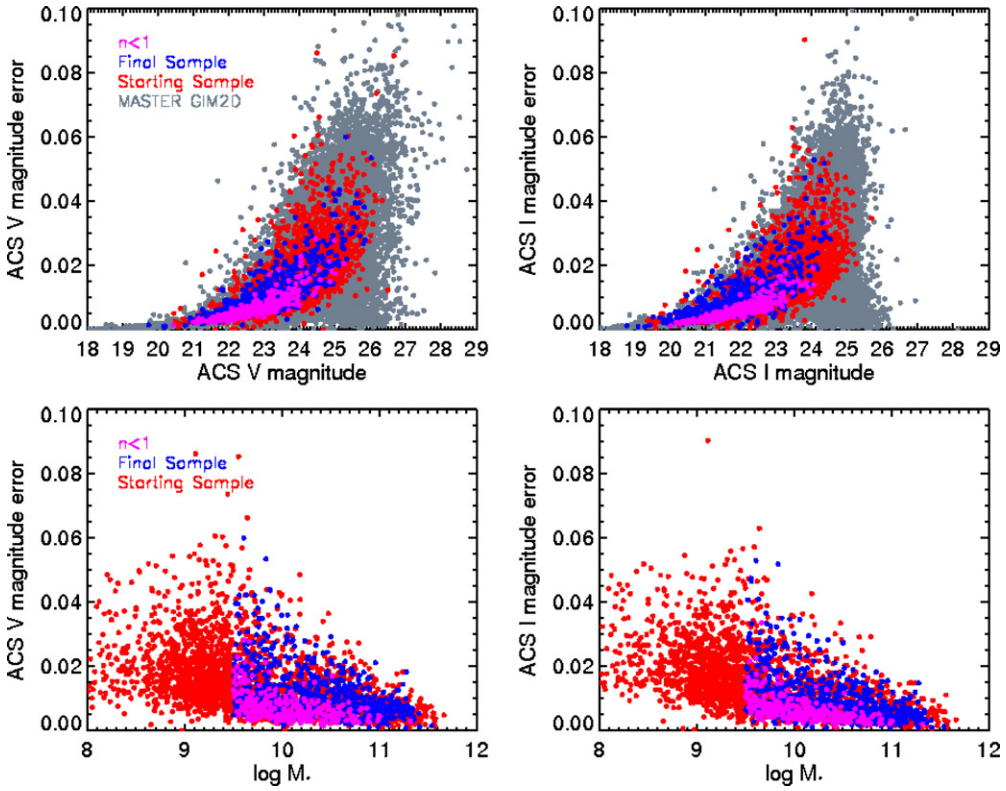

Figure 11. V and I magnitude errors as a function of V, I, and log M_*.
(A color version of this figure is available in the online journal.)

most important quantities are the GIM2D model *HST*/ACS V and I magnitudes since every structural measurement is based on them. Figure 11 plots the V and I 1σ errors as a function of V, I, and log M_*. These errors are confidence limits derived through full Monte Carlo propagations of the parameter probability distributions computed by GIM2D (Simard et al. 2002).

Shown are the master GIM2D catalog (gray), "starting" sample (red), "final" sample (blue), and galaxies within the "final" sample with Sérsic indices $n < 1$ (pink). The 5σ limiting magnitudes for the *HST*/ACS images are $V = 26.23$ and $I = 25.61$, consistent with the master GIM2D distribution. Within our "final" sample, the limits of the magnitude distributions are $\approx$0.5 mag and $\approx$1.0 mag brighter than those limits, respectively. And most importantly, the V and I magnitude errors at the mass and magnitude limit of the "final" sample are small, $\leqslant$0.06 mag, with the majority $\leqslant$0.03 mag.

To further illustrate the quality of the "final" sample's GIM2D fits, we plot in Figure 12 the 1σ error of the Sérsic index, fractional 1σ error of the effective radius, and the 1σ error of the bulge-to-total ratio B/T (in the I band) as a function of V, I, and M_*. The errors of the Sérsic index measurements are almost all $\leqslant$0.2. A typical late-type galaxy has $n \sim 1$, while a typical early-type galaxy has $n \sim 4$. An error of 0.2 on n will not affect this division, and hence these errors are tolerable. The errors on the effective radius measurements are presented as fractional errors, i.e., 1σ effective radius error divided by the effective radius. Note that these radii are semimajor axis effective radii and not circularized effective radii. The fractional errors are small: almost all are $\leqslant$6%. The errors on the B/T are almost all $\leqslant$0.05. Most star-forming, blue galaxies in our "starting" sample, which are presumably late-type, have $B/T \leqslant 0.10$, while most quiescent, red galaxies in our "starting" sample, which are presumably early-type, have $B/T \geqslant 0.40$. Thus, an error of 0.05 will not push blue galaxies to B/T values of red galaxies and vice versa. In summary, these plots demonstrate that our "final" sample contains quality GIM2D measurements down to the mass and magnitude limits of the "final" sample.

APPENDIX C

SÉRSIC INDEX BIAS?

One might be concerned that the Sérsic index may be sensitive to surface brightness and stellar mass. Figure 13 plots the Sérsic index against these quantities. The top row is the μ in V and I. The vertical green dot-dashed line represents the approximate edge of the "final" sample's surface brightness distribution as seen in Figure 10. The contours represent the number density of the master GIM2D catalog, which clearly shows that the majority of these galaxies have low n. At faint μ, the "starting" sample clearly has less $n > 3$ galaxies compared to the $n < 3$ population, but we would argue that this is a reflection of the universe, i.e., high-n galaxies generally have bright μ. For the "final" sample, however, this proportional dearth of $n > 3$, faint μ galaxies seen in the "starting" sample seems to have been greatly reduced.

We also plot the Sérsic index against stellar mass in the lower panel. At low stellar masses, the "starting" sample also has less high-n galaxies than low-n galaxies. However, this absence does not seem as severe as with faint μ. And within our "final" sample, it seems that this disparity in Sérsic populations has decreased. Moreover, it is important to note that even at the lowest masses, our "final" sample still contains Sérsic index values across the entire possible range, indicating that GIM2D does not preclude high-n fits for low-mass galaxies. In fact, the absolute count of galaxies with Sérsic index $n > 3$ in every mass range is approximately the same. Hence, there is

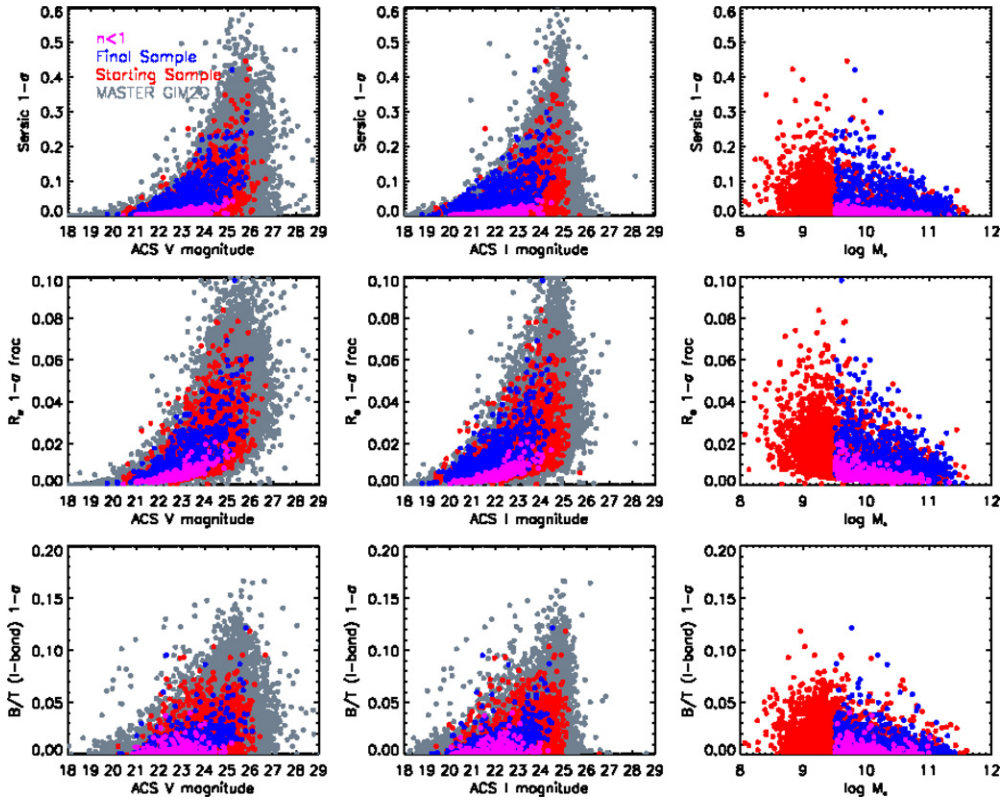

Figure 12. Sérsic index error, effective radius fractional error, and bulge-to-total ratio errors as a function of V, I, and $\log M_*$.
(A color version of this figure is available in the online journal.)

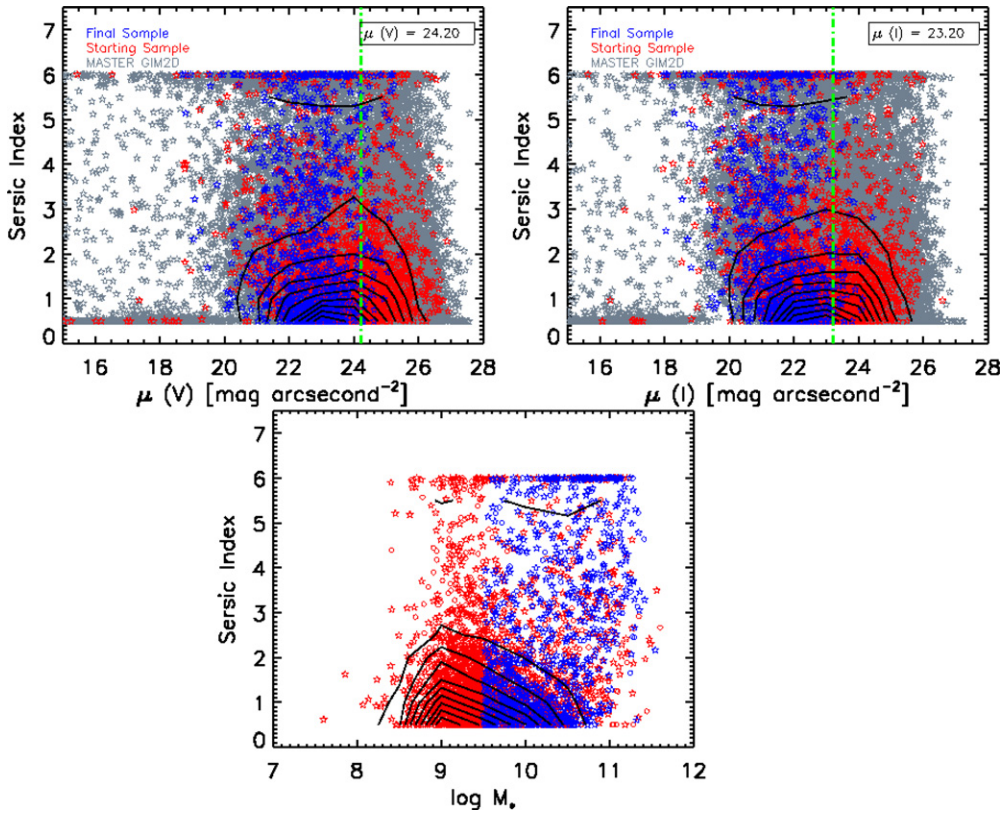

Figure 13. Sérsic index is plotted against $\mu(V)$ and $\mu(I)$ in the top row. Contours represent the number density of the GIM2D master sample in gray. The vertical green dot-dashed line represents the approximate edge of our "final" sample's surface brightness distribution (as seen in Figure 10). The bottom panel plots the Sérsic index against stellar mass. The "final" sample does not show a strong disparity of high- and low-n populations at faint (low) surface brightness (mass).
(A color version of this figure is available in the online journal.)

no predisposition against $n > 3$ galaxies in our "final" sample. The fact that our "final" sample has a large concentration of low-n galaxies is most likely due to the fact that there are many late-type galaxies at low masses.

One might wonder how the low-n galaxies fared near the limits of the data. As can be seen in Figure 13, the low-n galaxies make up a significant fraction of our "final" sample. To see the reliability of the measurements of these galaxies, we have highlighted this population ($n < 1$ galaxies in the "final" sample) in magenta in several of the previous figures, specifically, Figures 11 and 12. In most cases, these low-n galaxies have errors consistent with the rest of the population, i.e., low-n galaxies fare fine near the limits of our "final" sample.

REFERENCES

Abraham, R. G., Valdes, F., Yee, H. K. C., & van den Bergh, S. 1994, ApJ, 432, 75
Alexander, D. M., Swinbank, A. M., Smail, I., McDermid, R., & Nesvadba, N. P. H. 2010, MNRAS, 402, 2211
Allen, P. D., Driver, S. P., Graham, A. W., et al. 2006, MNRAS, 371, 2
Ammons, S. M., Rosario, D. J. V., Koo, D. C., et al. 2011, ApJ, 740, 3
Arnouts, S., Walcher, C. J., Le Fèvre, O., et al. 2007, A&A, 476, 137
Baldwin, J. A., Phillips, M. M., & Terlevich, R. 1981, PASP, 93, 5
Barmby, P., Huang, J.-S., Ashby, M. L. N., et al. 2008, ApJS, 177, 431
Barro, G., Pérez-González, P. G., Gallego, J., et al. 2011a, ApJS, 193, 13
Barro, G., Pérez-González, P. G., Gallego, J., et al. 2011b, ApJS, 193, 30
Bell, E. F. 2008, ApJ, 682, 355
Bell, E. F., & de Jong, R. S. 2001, ApJ, 550, 212
Bell, E. F., McIntosh, D. H., Barden, M., et al. 2004a, ApJ, 600, L11
Bell, E. F., Phleps, S., Somerville, R. S., et al. 2006, ApJ, 652, 270
Bell, E. F., van der Wel, A., Papovich, C., et al. 2012, ApJ, 753, 167
Bell, E. F., Wolf, C., Meisenheimer, K., et al. 2004b, ApJ, 608, 752
Bertin, E., & Arnouts, S. 1996, A&AS, 117, 393
Bezanson, R., van Dokkum, P. G., Franx, M., et al. 2011, ApJ, 737, L31
Bigiel, F., Leroy, A., Walter, F., et al. 2008, AJ, 136, 2846
Birnboim, Y., & Dekel, A. 2003, MNRAS, 345, 349
Birnboim, Y., & Dekel, A. 2011, MNRAS, 415, 2566
Blanton, M. R., Hogg, D. W., Bahcall, N. A., et al. 2003, ApJ, 594, 186
Blanton, M. R., & Roweis, S. 2007, AJ, 133, 734
Bluck, A. F. L., Conselice, C. J., Buitrago, F., et al. 2012, ApJ, 747, 34
Blumenthal, G. R., Faber, S. M., Primack, J. R., & Rees, M. J. 1984, Nature, 311, 517
Borch, A., Meisenheimer, K., Bell, E. F., et al. 2006, A&A, 453, 869
Bournaud, F., Jog, C. J., & Combes, F. 2007, A&A, 476, 1179
Bournaud, F., Juneau, S., Le Floc'h, E., et al. 2012, ApJ, 757, 81
Brammer, G. B., Whitaker, K. E., van Dokkum, P. G., et al. 2011, ApJ, 739, 24
Brinchmann, J., Charlot, S., White, S. D. M., et al. 2004, MNRAS, 351, 1151
Brown, M. J. I., Dey, A., Jannuzi, B. T., et al. 2007, ApJ, 654, 858
Bruzual, G., & Charlot, S. 2003, MNRAS, 344, 1000
Bundy, K., Ellis, R. S., Conselice, C. J., et al. 2006, ApJ, 651, 120
Bundy, K., Fukugita, M., Ellis, R. S., et al. 2009, ApJ, 697, 1369
Bundy, K., Scarlata, C., Carollo, C. M., et al. 2010, ApJ, 719, 1969
Cameron, E., Carollo, C. M., Oesch, P., et al. 2010, MNRAS, 409, 346
Cano-Diaz, M., Maiolino, R., Marconi, A., et al. 2012, A&A, 537, L8
Capaccioli, M. 1989, World of Galaxies (Le Monde des Galaxies; New York: Springer), 208
Catinella, B., Schiminovich, D., Kauffmann, G., et al. 2010, MNRAS, 403, 683
Cattaneo, A., Dekel, A., Devriendt, J., Guiderdoni, B., & Blaizot, J. 2006, MNRAS, 370, 1651
Ceverino, D., Dekel, A., & Bournaud, F. 2010, MNRAS, 404, 2151
Ciotti, L., Ostriker, J. P., & Proga, D. 2009, ApJ, 699, 89
Coil, A. L., Newman, J. A., Kaiser, N., et al. 2004, ApJ, 617, 765
Coil, A. L., Weiner, B. J., Holz, D. E., et al. 2011, ApJ, 743, 46
Collister, A. A., & Lahav, O. 2004, PASP, 116, 345
Conroy, C., & Wechsler, R. H. 2009, ApJ, 696, 620
Conselice, C. J. 2006, ApJ, 638, 686
Cooper, M. C., Aird, J. A., Coil, A. L., et al. 2011, ApJS, 193, 14
Cooper, M. C., Griffith, R. L., Newman, J. A., et al. 2012, MNRAS, 419, 3018
Cortese, L., & Hughes, T. M. 2009, MNRAS, 400, 1225
Couch, W. J., & Sharples, R. M. 1987, MNRAS, 229, 423
Cowie, L. L., Songaila, A., Hu, E. M., & Cohen, J. G. 1996, AJ, 112, 839
Cox, T. J., Jonsson, P., Somerville, R. S., Primack, J. R., & Dekel, A. 2008, MNRAS, 384, 386
Croton, D. J., Springel, V., White, S. D. M., et al. 2006, MNRAS, 365, 11
Davis, M., Faber, S. M., Newman, J., et al. 2003, Proc. SPIE, 4834, 161
Davis, M., Guhathakurta, P., Konidaris, N. P., et al. 2007, ApJ, 660, L1
De Propris, R., Stanford, S. A., Eisenhardt, P. R., Holden, B. P., & Rosati, P. 2007, AJ, 133, 2209
Dekel, A., & Birnboim, Y. 2006, MNRAS, 368, 2
Dekel, A., Sari, R., & Ceverino, D. 2009, ApJ, 703, 785
Domínguez, A., Primack, J. R., Rosario, D. J., et al. 2011, MNRAS, 410, 2556
Dressler, A., & Gunn, J. E. 1983, ApJ, 270, 7
Driver, S. P., Allen, P. D., Graham, A. W., et al. 2006, MNRAS, 368, 414
Driver, S. P., Allen, P. D., Liske, J., & Graham, A. W. 2007, ApJ, 657, L85
Drory, N., & Fisher, D. B. 2007, ApJ, 664, 640
Elmegreen, B. G., Bournaud, F., & Elmegreen, D. M. 2008, ApJ, 688, 67
Fabello, S., Catinella, B., Giovanelli, R., et al. 2011, MNRAS, 411, 993
Faber, S. M., Phillips, A. C., Kibrick, R. I., et al. 2003, Proc. SPIE, 4841, 1657
Faber, S. M., Willmer, C. N. A., Wolf, C., et al. 2007, ApJ, 665, 265
Farrah, D., Urrutia, T., Lacy, M., et al. 2012, ApJ, 745, 178
Fisher, D. B., & Drory, N. 2008, AJ, 136, 773
Fisher, D. B., & Drory, N. 2011, ApJ, 733, L47
Fisher, D. B., Drory, N., & Fabricius, M. H. 2009, ApJ, 697, 630
Forbes, J., Krumholz, M. R., & Burkert, A. 2012, ApJ, 754, 48
Franx, M., van Dokkum, P. G., Schreiber, N. M. F., et al. 2008, ApJ, 688, 770
Gebhardt, K., Bender, R., Bower, G., et al. 2000, ApJ, 539, L13
Gebhardt, K., Faber, S. M., Koo, D. C., et al. 2003, ApJ, 597, 239
Gerke, B. F., Newman, J. A., Davis, M., et al. 2005, ApJ, 625, 6
Gonçalves, T. S., Martin, D. C., Menéndez-Delmestre, K., Wyder, T. K., & Koekemoer, A. 2012, ApJ, 759, 67
Goto, T., Yamauchi, C., Fujita, Y., et al. 2003, MNRAS, 346, 601
Governato, F., Brook, C. B., Brooks, A. M., et al. 2009, MNRAS, 398, 312
Governato, F., Willman, B., Mayer, L., et al. 2007, MNRAS, 374, 1479
Guedes, J., Callegari, S., Madau, P., & Mayer, L. 2011, ApJ, 742, 76
Gunn, J. E., & Gott, J. R., III. 1972, ApJ, 176, 1
Hopkins, P. F., Bundy, K., Croton, D., et al. 2010a, ApJ, 715, 202
Hopkins, P. F., Bundy, K., Hernquist, L., Wuyts, S., & Cox, T. J. 2010b, MNRAS, 401, 1099
Hopkins, P. F., Bundy, K., Murray, N., et al. 2009a, MNRAS, 398, 898
Hopkins, P. F., Cox, T. J., Younger, J. D., & Hernquist, L. 2009b, ApJ, 691, 1168
Hopkins, P. F., Hernquist, L., Cox, T. J., Dutta, S. N., & Rothberg, B. 2008, ApJ, 679, 156
Huang, J.-S., Cowie, L. L., Gardner, J. P., et al. 1997, ApJ, 476, 12
Ilbert, O., Salvato, M., Le Floc'h, E., et al. 2010, ApJ, 709, 644
Im, M., Faber, S. M., Gebhardt, K., et al. 2001, AJ, 122, 750
Im, M., Simard, L., Faber, S. M., et al. 2002, ApJ, 571, 136
Inoue, S., & Saitoh, T. R. 2012, MNRAS, 422, 1902
Jogee, S., Barazza, F. D., Rix, H.-W., et al. 2004, ApJ, 615, L105
Kang, X., Jing, Y. P., Mo, H. J., & Böumlrner, G. 2005, ApJ, 631, 21
Kannappan, S. J., Guie, J. M., & Baker, A. J. 2009, AJ, 138, 579
Kauffmann, G., Heckman, T. M., De Lucia, G., et al. 2006, MNRAS, 367, 1394
Kauffmann, G., Heckman, T. M., White, S. D. M., et al. 2003, MNRAS, 341, 54
Kennicutt, R. C., Jr. 1989, ApJ, 344, 685
Kereš, D., Katz, N., Weinberg, D. H., & Davé, R. 2005, MNRAS, 363, 2
Khochfar, S., & Ostriker, J. P. 2008, ApJ, 680, 54
Koo, D. C., Simard, L., Willmer, C. N. A., et al. 2005, ApJS, 157, 175
Kormendy, J., & Kennicutt, R. C. 2004, ARA&A, 42, 603
Krumholz, M. R., Dekel, A., & McKee, C. F. 2012, ApJ, 745, 69
Krumholz, M. R., Leroy, A. K., & McKee, C. F. 2011, ApJ, 731, 25
Laird, E. S., et al. 2009, VizieR Online Data Catalog, 218, 102
Larson, R. B., Tinsley, B. M., & Caldwell, C. N. 1980, ApJ, 237, 692
Lee, G.-H., Park, C., Lee, M. G., & Choi, Y.-Y. 2012, ApJ, 745, 125
Lin, H., Yee, H. K. C., Carlberg, R. G., et al. 1999, ApJ, 518, 533
Lin, L., Koo, D. C., Weiner, B. J., et al. 2007, ApJ, 660, L51
Lin, L., Patton, D. R., Koo, D. C., et al. 2008, ApJ, 681, 232
Lotz, J. M., Davis, M., Faber, S. M., et al. 2008a, ApJ, 672, 177
Lotz, J. M., Jonsson, P., Cox, T. J., & Primack, J. R. 2008b, MNRAS, 391, 1137
Lotz, J. M., Jonsson, P., Cox, T. J., et al. 2011, ApJ, 742, 103
Magorrian, J., Tremaine, S., Richstone, D., et al. 1998, AJ, 115, 2285
Maier, C., Lilly, S. J., Zamorani, G., et al. 2009, ApJ, 694, 1099
Martig, M., Bournaud, F., Teyssier, R., & Dekel, A. 2009, ApJ, 707, 250
Martin, D. C., Wyder, T. K., Schiminovich, D., et al. 2007, ApJS, 173, 342
Masters, K. L., Nichol, R. C., Hoyle, B., et al. 2011, MNRAS, 411, 2026
Menanteau, F., Abraham, R. G., & Ellis, R. S. 2001, MNRAS, 322, 1
Mendez, A. J., Coil, A. L., Lotz, J., et al. 2011, ApJ, 736, 110
Mihos, J. C., & Hernquist, L. 1994, ApJ, 437, L47
Moore, B., Katz, N., Lake, G., Dressler, A., & Oemler, A. 1996, Nature, 379, 613
More, S., van den Bosch, F. C., Cacciato, M., et al. 2011, MNRAS, 410, 210

Morganti, R., de Zeeuw, P. T., Oosterloo, T. A., et al. 2006, MNRAS, 371, 157
Murray, N., Quataert, E., & Thompson, T. A. 2005, ApJ, 618, 569
Naab, T., & Trujillo, I. 2006, MNRAS, 369, 625
Nair, P. B., & Abraham, R. G. 2010, ApJ, 714, L260
Newman, J. A., Cooper, M. C., Davis, M., et al. 2012, arXiv:1203.3192
Noeske, K. G., Weiner, B. J., Faber, S. M., et al. 2007, ApJ, 660, L43
Noguchi, M. 1999, ApJ, 514, 77
Noordermeer, E., van der Hulst, J. M., Sancisi, R., Swaters, R. A., & van Albada, T. S. 2005, A&A, 442, 137
Okamoto, T., Eke, V. R., Frenk, C. S., & Jenkins, A. 2005, MNRAS, 363, 1299
Oosterloo, T., Morganti, R., Crocker, A., et al. 2010, MNRAS, 409, 500
Peng, Y.-j., Lilly, S. J., Kovač, K., et al. 2010, ApJ, 721, 193
Peng, Y.-j., Lilly, S. J., Renzini, A., & Carollo, M. 2012, ApJ, 757, 4
Pierce, C. M., Lotz, J. M., Salim, S., et al. 2010, MNRAS, 408, 139
Poggianti, B. M., Smail, I., Dressler, A., et al. 1999, ApJ, 518, 576
Quintero, A. D., Hogg, D. W., Blanton, M. R., et al. 2004, ApJ, 602, 190
Rees, M. J., & Ostriker, J. P. 1977, MNRAS, 179, 541
Robaina, A. R., Bell, E. F., van der Wel, A., et al. 2010, ApJ, 719, 844
Roberts, M. S., & Haynes, M. P. 1994, ARA&A, 32, 115
Robertson, B., Bullock, J. S., Cox, T. J., et al. 2006, ApJ, 645, 986
Saintonge, A., Kauffmann, G., Wang, J., et al. 2011, MNRAS, 415, 61
Salim, S., Charlot, S., Rich, R. M., et al. 2005, ApJ, 619, L39
Salim, S., Fang, J. J., Rich, R. M., Faber, S. M., & Thilker, D. A. 2012, ApJ, 755, 105
Salim, S., & Rich, R. M. 2010, ApJ, 714, L290
Salim, S., Rich, R. M., Charlot, S., et al. 2007, ApJS, 173, 267
Sanders, D. B., Soifer, B. T., Elias, J. H., et al. 1988, ApJ, 325, 74
Schawinski, K., Lintott, C., Thomas, D., et al. 2009, MNRAS, 396, 818
Schawinski, K., Thomas, D., Sarzi, M., et al. 2007, MNRAS, 382, 1415
Schaye, J. 2004, ApJ, 609, 667
Schiminovich, D., Catinella, B., Kauffmann, G., et al. 2010, MNRAS, 408, 919
Schiminovich, D., Wyder, T. K., Martin, D. C., et al. 2007, ApJS, 173, 315
Sersic, J. L. 1968, Atlas de Galaxias Australes (Cordoba, Argentina: Observatorio Astronomico)
Shen, S., Mo, H. J., White, S. D. M., et al. 2003, MNRAS, 343, 978
Sheth, K., Elmegreen, D. M., Elmegreen, B. G., et al. 2008, ApJ, 675, 1141
Silk, J. 1977, ApJ, 211, 638
Simard, L., Willmer, C. N. A., Vogt, N. P., et al. 2002, ApJS, 142, 1
Simkin, S. M., Su, H. J., & Schwarz, M. P. 1980, ApJ, 237, 404
Sirianni, M., Jee, M. J., Benítez, N., et al. 2005, PASP, 117, 1049
Springel, V., Di Matteo, T., & Hernquist, L. 2005, ApJ, 620, L79
Springel, V., & Hernquist, L. 2005, ApJ, 622, L9
Strateva, I., Ivezić, Ž., Knapp, G. R., et al. 2001, AJ, 122, 1861
Taylor, E. N., Franx, M., Brinchmann, J., van der Wel, A., & van Dokkum, P. G. 2010, ApJ, 722, 1
Thomas, D., Maraston, C., Bender, R., & Mendes de Oliveira, C. 2005, ApJ, 621, 673
Toomre, A., & Toomre, J. 1972, ApJ, 178, 623
van Driel, W., & van Woerden, H. 1991, A&A, 243, 71
Wake, D. A., Franx, M., & van Dokkum, P. G. 2012a, arXiv:1201.1913
Wake, D. A., van Dokkum, P. G., & Franx, M. 2012b, ApJ, 751, L44
Weiner, B. J., Coil, A. L., Prochaska, J. X., et al. 2009, ApJ, 692, 187
Weiner, B. J., Phillips, A. C., Faber, S. M., et al. 2005, ApJ, 620, 595
Williams, R. J., Quadri, R. F., Franx, M., van Dokkum, P., & Labbé, I. 2009, ApJ, 691, 1879
Woo, J., Dekel, A., Faber, S. M., et al. 2012, arXiv:1203.1625
Wuyts, S., Förster Schreiber, N. M., van der Wel, A., et al. 2011, ApJ, 742, 96
Wuyts, S., Labbé, I., Schreiber, N. M. F., et al. 2008, ApJ, 682, 985
Xu, C. K., Zhao, Y., Scoville, N., et al. 2012, ApJ, 747, 85
Yan, R., Ho, L. C., Newman, J. A., et al. 2011, ApJ, 728, 38
Yang, Y., Zabludoff, A. I., Zaritsky, D., & Mihos, J. C. 2008, ApJ, 688, 945
Zheng, X. Z., Bell, E. F., Papovich, C., et al. 2007, ApJ, 661, L41